A STUDY ON ENERGY-STORAGE MATERIALS FOR SUPERCAPACITOR APPLICATIONS

YU KUN

MPhil

The Hong Kong Polytechnic University

2019

The Hong Kong Polytechnic University

Department of Applied Physics

A Study on Energy-Storage Materials for Supercapacitor Applications

YU Kun

A thesis submitted in partial fulfillment of the requirements

for the degree of Master of Philosophy

August 2018

CERTIFICATE OF ORIGINALITY

I hereby declare that this thesis is my own work and that, to the best of my knowledge and belief, it reproduces no material previously published or written, nor material that has been accepted for the award of any other degree or diploma, except where due acknowledgement has been made in the text.

_____ (Signed)

Yu Kun
_____ (Name of student)

Abstract

Supercapacitors have attracted extremely high interest from scientists and engineers due to their broad applications in portable electronics, electric vehicles and flexible systems. They have remarkable properties compared to batteries such as fast charging and discharging, high power density, long cycling life and safe operation. Electrode materials and structure could greatly affect the performance of a supercapacitor. In this research, various methods are investigated to enhance the supercapacitors performance.

The study began on $MnCo_2S_4$-$NiCo(OH)_2$ core-shell nanocomposite for high-performance solid-state supercapacitor applications. Transition metal sulfides, for example CoS_x, NiS_x and MnS_x, possessing high electrochemical performance for supercapacitors have attracted great attention in recent years. A ternary metal sulphide nanostructure $MnCo_2S_4$ was designed and fabricated to combine the advantages of CoS_x and MnS_x for supercapacitors. $MnCo_2S_4$ nanostructure can serve as porous platforms for loading a large amount of additional active materials, enabling fast electron conduction and ion diffusion. To further improve the electrochemical performance, Ni-Co hydroxide nanosheet was deposited on the surface of $MnCo_2S_4$ to form a hierarchical core-shell structure. Core-shell structure is a promising electrode configuration due to its rich redox reaction sites and sufficient contact area between electrode and electrolyte. The electrode based on the $MnCo_2S_4$@$NiCo(OH)_2$ core-shell nanocomposite showed excellent areal capacitance and the symmetric supercapacitor fabricated with this electrode exhibited

high energy density, power density and good rate capability.

With a view to promoting the electrochemical behavior, a ternary metal sulphide was then used as a shell material and grown on the surface of $MnCo_2S_4$ by a simple electrochemical deposition to form a $MnCo_2S_4$@Ni-Co-S (MCS@NCS) core-shell nanostructure. Due to the synergistic effect of core and shell materials, the electrochemical performance of the core-shell hybrid electrode could be enhanced significantly. The as-prepared MCS@NCS core-shell hybrid electrode displayed ultrahigh areal capacitance (10.14 F/cm^2 at a current density of 1 mA/cm^2). The morphology, crystallinity, specific surface area and porosity of the electrode materials were characterized by scanning electron microscopy, transmission electron microscopy, x-ray diffraction and Brunauer-Emmett-Teller N_2 adsorption/desorption measurement system. Moreover, an asymmetric supercapacitor using Ni foam@MCS@NCS as the positive electrode and Ni foam@activated carbon as the negative electrode was fabricated with 6 M KOH as the electrolyte. The fabricated asymmetric supercapacitor showed large operating voltage (1.65 V), excellent energy density (7.26 Wh/m^2) and durability, revealing its great potential applications as an efficient energy storage device.

Flexible supercapacitors have attracted significant attention in recent years due to their potential application in miniaturized, portable, flexible and wearable electronics. In view of this, flexible solid-state supercapacitors using paper-based electrodes for energy storage were investigated. A soaking and electrodeposition method was introduced to coat carbon nanotubes (CNTs) and nickel cobalt sulphide (NCS) on a filter paper to prepare flexible paper-based electrodes. Paper was chosen as the substrate due to its

notable features including wide availability, lightweight, flexibility, low cost, recyclability and environmental benignancy. These Paper-CNT-NCS hybrid electrodes and the solid-state electrolyte were assembled together to form the supercapacitor. By combining the advantages of CNT and NCS, the as-fabricated solid-state flexible supercapacitor demonstrated great potential as an energy storage component for flexible electronic applications.

Finally, for the realization of low-cost, scalable and printable energy storage devices, interdigitated planar structure of flexible and solid-state symmetric supercapacitors with active electrode material consisting of Mn-Co deposited by inkjet printing was developed. The interdigitated structure with finger electrodes has many advantages including large surface area, short migration distance of ions and small internal resistance. The correlation between the dimensions of the interdigitated electrodes and the electrochemical performance of the supercapacitors was studied. Compared to the conventional synthesis methods such as electrochemical deposition and hydrothermal treatment, inkjet printing method allows more large-scale and rapid production for industrial applications.

List of Publications

1. K. Yu, W.M. Tang, J.Y. Dai, "Double-layer $MnCo_2S_4$@Ni-Co-S core/shell nanostructure on nickel foam for high-performance supercapacitor", Physica Status Solidi A: Applications and Materials Science, pp. 1800147-1-9, 2018.
2. K. Yu, W.M. Tang, J.Y. Dai, "Flexible Solid-state Supercapacitors Using Paper-based Electrodes for Energy Storage" in 2018 IEEE International Conference on Electron Devices and Solid-State Circuits, 2018.
3. K. Yu, W.M. Tang, J.Y. Dai, "A Study on $MnCo_2S_4$@$NiCo(OH)_2$ Core-Shell Nanocomposite for High-Performance Solid-State Supercapacitor Applications," in 2017 IEEE International Conference on Electron Devices and Solid-State Circuits, 2017.

Acknowledgement

When I am going to finish my study and research life in PolyU, I would like to express my sincere gratitude to the people who give me trust, support, instruction, inspiration and constructive suggestions.

Firstly, I would like to thank my primary supervisor Dr. Tang Wing Man who gives me an opportunity to study for an MPhil degree and offers me plenty of great suggestions, professional research information and good environment for research and study. She teaches me how to be a good researcher with her nice and patient characters. Her hard-working attitude on research also drives me to pursue a higher goal in the future. I also want to thank my co-supervisor Prof. Dai Jiyan and all the staff in Department of Applied Physics who offer me great and selfless support on research.

I would like to thank my good friends in Reading Club where I gain friendship and happiness.

I would also like to thank my friend Mr. Willis Ho in PolyU who has nice and interesting personalities and offers me great help on both research and life.

More importantly, I would like to express my great gratitude to my parents who always give me great support when I am in trouble. This thesis is dedicated to my family.

Table of Contents

Chapter 1
Introduction

1.1 Overview

In the past few decades, with the rapid development of industry and the rise in population, many important issues such as energy crisis, global warming and pollution are threatening the human being and becoming the obstacles for the sustainability of society. The key to address the ecological and energy problems is to find cleaner energy sources and energy storage methods with better efficiency [1-3]. Having highly efficient, stable, reliable and safe energy storage devices and systems are very important and useful in our daily life as they can solve the intermittent power supply problem of many clean renewable energy sources such as wind energy, solar energy and tidal energy [2-4]. In addition, energy storage technology is applied to kinetic energy recovery systems in electric vehicles during the braking process and many marine, military, electronics and aerospace applications [3]. Considerable efforts are put into the development of high-performance energy storage devices and systems to meet the strict energy requirements.

Among various energy storage technologies, batteries and supercapacitors are at the forefront. However, batteries still suffer from some limitations and problems for example low power density, short cycling life, slow charge/discharge rate, abrupt failure and safety concern. Moreover, batteries are not easy to integrate with other

electronic circuits and be minimized for on-chip energy storage. On the contrary, supercapacitors (also called ultra-capacitors or electrochemical capacitors) have aroused a great deal of interest from engineers and scientists and been applied in many industries due to their remarkable characteristics such as high power density, extremely long cycle life, fast charging, and safe operation [4, 5]. They are particularly suitable for applications demanding fast response and quick charges. Moreover, they can be functioned at low temperatures (-40 ^{o}C) and easily combined with different nanogenerators to form a self-powered energy system. Although the energy density of supercapacitors is higher than that of conventional capacitors, it is lower than that of batteries [6, 7]. If the energy density of the supercapacitors can be enhanced without scarifying cycling life and power density, batteries can be replaced by supercapacitors in the field of energy storage.

1.2 Classification of Supercapacitors

A supercapacitor typically consists of two electrodes, an electrolyte and a separator to avoid short circuit [8]. Based on the energy storage mechanism, supercapacitors can be mainly divided into two types: electric double-layer capacitors (EDLCs) and pseudocapacitors [5, 6].

1.2.1 Electric Double-Layer Capacitors

Figure 1.1 shows a schematic diagram of an electric double-layer capacitor. The electrolyte is full of positive and negative ions. When a voltage is applied to the electrodes during the charging process, the cations (positively charged) in the electrolyte are accumulated to the negative electrode while the negatively charged anions are attracted to the positive electrode. Two electric double-layers are generated between the electrodes and the electrolyte and can be regarded as two capacitors connected in series. The capacitance in the electric double-layer called the electric double layer capacitance C_{dl} can be simply calculated by the following formula depicted by von Helmholtz [9]:

$$C_{dl} = \varepsilon_0 \varepsilon_r A/d \tag{1.1}$$

where A is the surface area of the electrode, d the thickness of the electric double layer, ε_0 the vacuum dielectric constant and ε_r the dielectric constant of the electrolyte. Generally, the electric double layer thickness (the charge separation at the electrode/

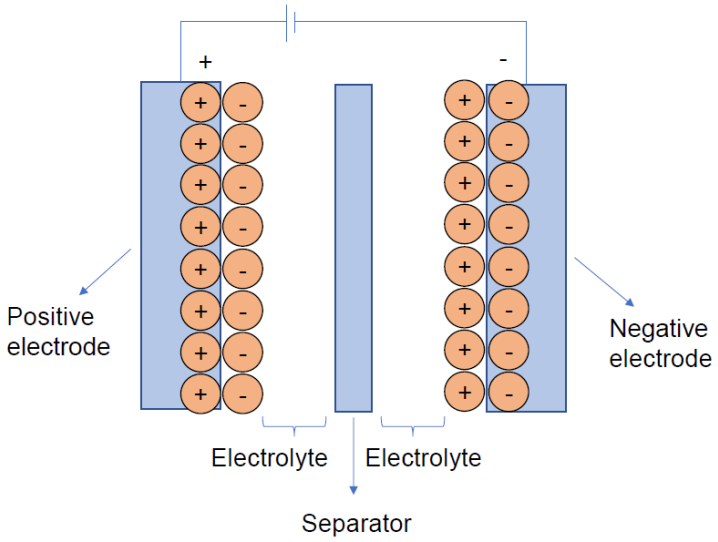

Figure 1.1. Schematic diagram of an electric double-layer capacitor.

electrolyte interface) can be 0.2 – 1 nm [10]. The charge-discharge process in EDLCs is a simple physical process involving charge accumulation and separation at the electrode-electrolyte interfaces without any redox reactions involved. The advantages of the EDLCs are long cycling life, high power density and good rate capability [2].

The electric double layer in EDLCs can be described by many theories and models such as the Helmholtz model, Gouy–Chapman model and Stern model [11]. The Helmholtz model is the first and simplest model for electric double layer that illustrates the charge distribution in a double layer interface. In this model, the charges at the surface of the electrode are balanced by the opposite-polarity electrolyte ions at an atomic distance from the electrode surface as shown in Figure 1.2a. However, this theory may not be enough to explain the phenomenon observed in reality because the thermal fluctuation in the electrolyte has not been taken into consideration [11]. This Helmholtz model was later revised by Gouy and Chapman and the modified model was named as Gouy-Chapman model or diffuse model. In Gouy-Chapman model, there is a diffuse layer due to the scattering of the electrolyte ions caused by thermal motion as shown in Figure 1.2b. The concentration of ions in the electrolyte solution near the surface of electrode follows a Boltzmann distribution. The thickness of the diffuse layer depends on the temperature, the electrolyte concentration and the permittivity of the electrolyte. However, the Gouy-Chapman model still may not be adequate to describe the real situation because it assumes that the electrolyte ions can come near to the electrode surface without limit. In view of

this, Stern developed a new model for ion distribution called the Stern model which is a combination of Helmholtz model and Gouy-Chapman model. As shown in Figure 1.2c, there are two layers in the Stern model: Stern layer (also called compact layer) and diffuse layer. In the Stern layer, there are two planes: inner Helmholtz plane (IHP) and the outer Helmholtz plane (OHP). Electrolytic ions are strongly adsorbed by the electrode in the Stern layer and denoted as absorbed ions. In the Stern layer, there are anions (specifically absorbed ions) in IHP and cations (non-specifically absorbed ions) in OHP [9].

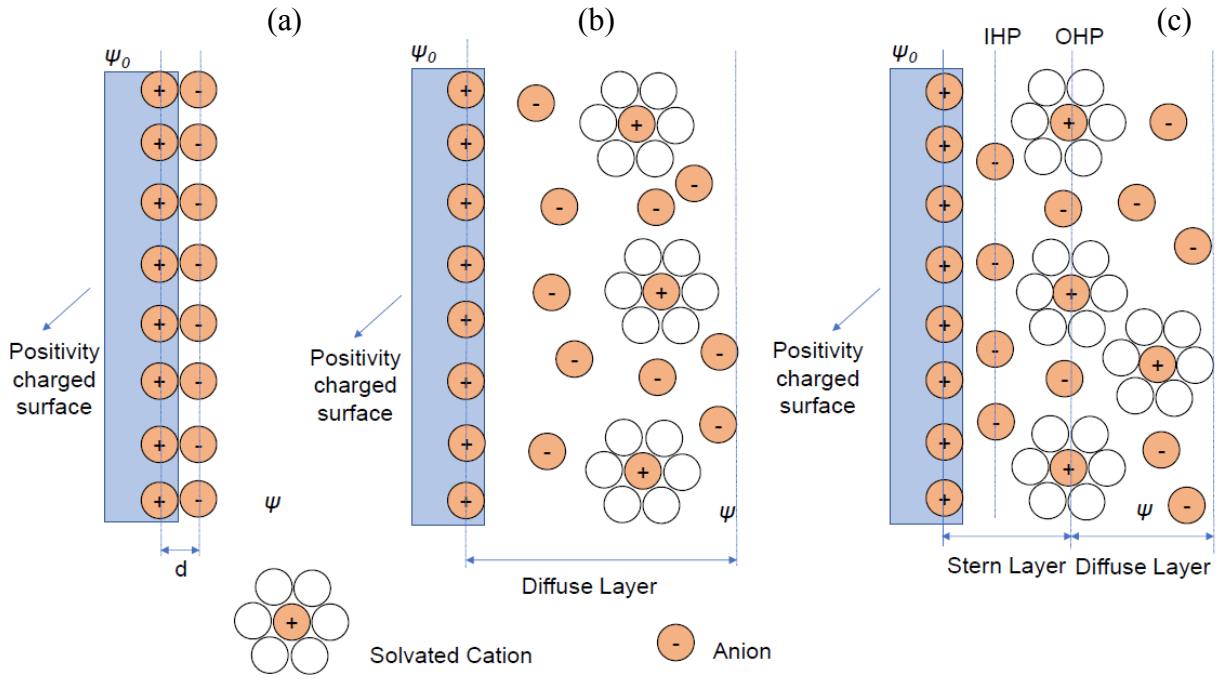

Figure 1.2. Models of double layer at the electrode-electrolyte interface: (a) Helmholtz model, (b) Gouy-Chapman model, and (c) Stern model. *d* is the charge separation distance depicted by the Helmholtz model. ψ_0 is the potential at the surface of the electrode and ψ is the potential at the interface of electrode and electrolyte. [9, 11]

Many factors can affect the capacitance of the EDLCs, such as the porosity, surface area and conductivity of the electrode. The electrode materials for EDLCs are mainly the carbon-based porous materials such as carbon nanotubes, activated carbon and graphene which store the charges in an electrochemical double-layer formed at the electrode/electrolyte interface.

1.2.2 Pseudocapacitors

The energy storage mechanism of pseudocapacitors is different from that of the electric double-layer capacitors. For the charge-discharge process in pseudocapacitors, a lot of fast and reversible faradaic redox reactions occur on the surface of the electrode for energy storage [12]. The ions in the electrolyte make charge-transfer with the electrode materials and different oxidation states of the electrode materials occur during the faradaic reactions [13-15]. The faradaic redox reactions at the electrode surface create the pseudocapacitance C_{pd} which can be expressed as follows:

$$C_{pd} = dQ/dV \tag{1.2}$$

where dQ is change in charge quantity originated from the faradaic redox reaction and dV is the change in potential of the electrode. The pseudocapacitance is usually 10-100 times higher than that of the electrical double layer capacitance. However, the pseudocapacitors have lower power capability than EDLCs due to relatively low conductivity [13]. Most of the pseduocapacitors are based on faradaic materials

(pseudocapacitive materials) including metal oxides and conducting polymers which can store charges based on redox reactions at their surfaces. A hybrid supercapacitor which combines the advantages of both EDLC and pseudocapacitor can be formed by utilizing one electric double-layer electrode and one pseudo-capacitive electrode in a cell [8, 14]. This asymmetric configuration can improve the electrochemical performance of a supercapacitor such as the operating voltage, capacitance, energy density and power density. The classification of supercapacitors is summarized in Figure 1.3.

1.3 Materials for Supercapacitors

The electrode materials for supercapacitors could be divided into two groups according to their charge storage mechanisms: (1) carbon-based materials and (2) faradaic materials. Through the efforts made by the researchers all around the world,

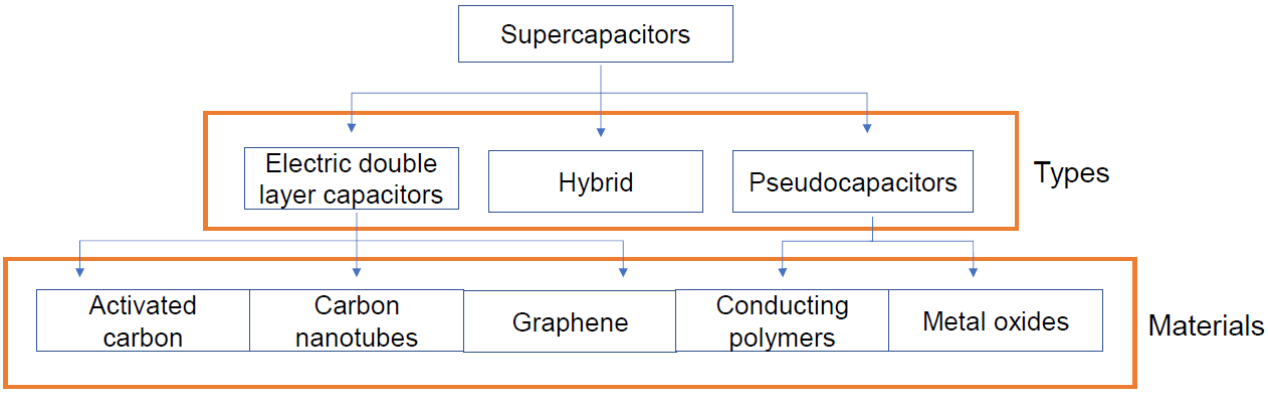

Figure 1.3. Classification of supercapacitors. [16]

plenty of materials can be used to make electrodes for different supercapacitor applications. The capacitance of supercapacitors can come from the electrical double layer capacitance and/or faradic pseudo or redox capacitance depending on the electrode materials.

1.3.1 Carbon-Based Materials

Carbon-based materials such as activated carbon (AC), carbon nanotubes (CNTs) and graphene are commonly used for EDLCs. They have many advantages such as [17]:

1. Good physical and chemical properties including high stability, large surface area, good conductivity, inert electrochemically, non-toxic, lightweight, and compatibility with other materials.
2. Low cost and abundance.
3. Easy availability of various forms such as nanoparticles, nanorods, nanoframeworks, powders, nanotubes, nanosheets, nanowires, nanoflowers, composites and fibers.
4. Ideal skeleton for loading other electrode materials.
5. Broad operating temperature range.
6. Controllability of pore size, shape and distribution.

Activated carbon

Activated carbons are most widely used in the electrode of supercapacitors due to their ease of fabrication, huge amount in nature and good electrical performance [18]. ACs are produced by carbonization of precursors followed by chemical and/or physical activation [19-21]. There are many precursors for the synthesis of ACs such as wood, flower, pitch, nutshell, starch, coal, microbeads, bamboo and polymers [22-24]. Chemical activation is generally performed at a temperature between 400 ^{o}C and 700 ^{o}C together with activating agent. Potassium hydroxide is an example of activating agent. Physical activation is usually conducted at higher temperatures (700 ^{o}C – 1200 ^{o}C) with gas flow during the treatment [9]. The porosity, surface area and electrochemical properties of activated carbons are strongly influenced by the precursors, activation methods and activation conditions including temperature, time, gas and the amount of activating agent [25].

Although AC has a large surface area of 3000 m^2/g, the measured capacitance of activated carbon is significantly smaller than its theoretical capacitance [25-27]. This indicates that not all the pores in the porous AC can be accessed by the electrolyte ions to form the electrical double layer [28]. This phenomenon shows that surface area is not the only factor that can affect the electrical double layer capacitance. Pore distribution, size and shape are also very important to affect the electrochemical performance [29].

The electrolyte can also determine the capacitance of AC. Previous reports show that the capacitance of AC in organic electrolyte is lower than that in aqueous

electrolyte. The possible reason is the different effective size of ions in aqueous solution and organic solution [12, 30, 31]. It was found that maximum double layer capacitance can be achieved by matching the pore sizes of AC with the sizes of electrolytic ions [32]. Adding functional groups on the AC surface (surface functionalization) is also a promising method to increase the capacitance of AC because the functional groups can offer extra pseudo capacitance.

Carbon nanotube

Carbon nanotubes (CNTs) are commonly used in many types of energy devices such as Li-ion batteries, fuel cells and supercapacitors. CNTs have great characteristics such as durable, flexible, high stability (mechanical and chemical) and good electrical conductivity [33]. They can be split into single-walled CNTs (SWNTs) or multi-walled CNTs (MWNTs). Both of them are extensively studied for high-performance energy-storage applications. An *et al*. reported that an electrode with SWNTs exhibited a capacitance of 180 F/g and a supercapacitor based on the SWNT electrodes has a power density of 20 kW/kg at an energy density of 7 Wh/kg in KOH electrolyte [34]. Comparing with AC, the main drawback of CNT is low capacitance due to small surface area (usually < 500 m^2/g), which limits the large-scale application of CNTs. The capacitance and surface area of CNTs can be increased by thermal and plasma treatments [34, 35]. Recent breakthroughs in massive fabrication

of CNTs have accelerated numerous novel applications of this attractive energy-storage material [36].

Graphene

Graphene is a honeycomb-like sheet with one-atom thick made of carbon atoms. It has great potential for energy storage applications. Graphene has good cycling capability, excellent thermal and electronic properties and large theoretical surface area of ~2620 m^2/g [16, 37, 38]. Graphene can be prepared by various methods such as hydrothermal reduction, photocatalytical reduction and microwave assisted exfoliation [39-41]. It has been reported that graphene is an outstanding carbon-based material for EDLCs because it can provide capacitance up to 550 F/g and the two major surfaces of graphene can be readily accessed by the electrolyte [42]. However, a major shortcoming of graphene is re-stacking and agglomeration which can reduce the surface area, capacitance and Coulombic efficiency [43].

1.3.2 Faradaic Materials

Faradaic materials for pseudocapacitors such as metal oxides and conducting polymers can deliver 10-1000 times higher capacitance than carbon-based materials for EDLCs. In addition, faradaic materials show higher energy density due to fast and reversible redox reactions at the surface [44].

Metal oxides

Many metal oxides have been used for making supercapacitor electrodes such as ruthenium oxide, iron oxide, bismuth oxide, nickel oxide, iridium oxide, tin oxide, vanadium oxide and manganese oxide. Among them, ruthenium oxide and manganese oxide are most widely investigated. The metal oxides used in energy-storage applications need to be conductive. The metal elements can show two or more oxidation states during the redox reactions. In addition, the protons can insert into the metal oxide lattice on reduction without any obstruction and also leave the oxide lattice freely on oxidation [8, 45].

Ruthenium oxide (RuO_2)

RuO_2 is a promising faradaic material due to its notable features such as wide voltage window, large surface area for redox reactions, availability of multiple oxidation states, good conductivity, very high theoretical capacitance, high rate capability, high thermal stability and long cycling life. The reactions of RuO_2 in different electrolyte solutions are different. In acidic electrolyte, a reversible electro-adsorption of protons and electron transfer happens on the RuO_2-electrode surface as described in the following equation [8, 46]:

$$RuO_2 + xH^+ + xe^- \leftrightarrow RuO_{2-x}OH_x \quad (1.3)$$

The oxidation states of Ru change from 2 to 4. However, the pseudocapacitive behavior of RuO_2 in an alkaline electrolyte is different. During the charging process,

the Ru is oxidized to RuO_4^{2-}, RuO_4^- and RuO_4 which are reduced back to ruthenium oxide in the discharging process [47, 48].

There are two key factors which determine the electrochemical performance of the RuO_2 electrode:

(1) Surface area. Most redox reactions occur at the surface of the electrode materials. Thus, larger surface area can offer more redox active sites for reactions [49]. Coating RuO_2 on a rough substrate with high surface area is one of the methods to increase the surface area of RuO_2 and thus the capacitance.

(2) Water content. The incorporation of water into ruthenium oxide can facilitate the proton transfer and improve the conductivity, leading to a higher capacitance. For example, hydrous ruthenium oxide ($RuO_2 \cdot 0.5H_2O$) has a capacitance of 900 F/g, which is much higher than that of $RuO_2 \cdot 0.3H_2O$ (29 F/g) and RuO_2 (0.5 F/g) [50, 51]. The fabrication conditions of RuO_2 can greatly affect the water content.

Although RuO_2 has many advantages, it is very expensive and environmentally unfriendly which limit its large-scale applications in industry [52].

Manganese oxide (MnO_2)

Due to the shortcomings of RuO_2, massive efforts have been made to find an alternative to ruthenium oxide. MnO_2 is a promising pesudocapacitive material which can replace RuO_2 in many energy-storage applications. MnO_2 has many attractive characteristics such as high theoretical capacitance (1100-1300 F/g), low

cost, non-toxic and environmental benignancy. MnO_2 has different morphologies through different synthesis methods. The pseudo-capacitance of MnO_2 is from faradaic redox reactions. Neutral electrolyte is often used for MnO_2-based supercapacitors as MnO_2 is not stable in strong acidic and alkali environments. The faradaic redox process at the surface of MnO_2 can be described by the following equation [53]:

$$MnO_2 + C^+ + e^- \longleftrightarrow MnO_2^- C^+ \quad (1.4)$$

where C^+ is the electrolyte cations such as K^+, Na^+ and Li^+. The oxidation state of Mn varies between 3 and 4 during the redox reactions. There are several properties that can influence pseudocapacitive performance of MnO_2 such as surface morphology, surface area, crystallinity and water content in the oxide.

Conducting Polymer

Apart from metal oxides, conducting polymer is another type of attractive faradaic material due to its low cost, environmentally friendly, high conductivity, wide potential window, ease of processing and high capacitance [54, 55]. Polyanilane, polypyrrol and polythiophene are common conducting polymers for supercapacitor applications. Faradaic redox reactions provide the main capacitance for the conducting polymer-based electrode. Ions in the electrolyte insert into the polymer skeleton during oxidation and come out into the electrolyte during reduction. In

addition, phase changes are not involved during the redox reactions. Hence, the charge-discharge process is very reversible.

Conducting polymer can be classified into “p-doped” polymer and “n-doped” polymer according to the charged situation. “p-doped” polymer is positively charged by oxidation and “n-doped” polymer is negatively charged by reduction. Generally, the conducting polymer-based supercapacitors have three structures [56, 57]:

1. p-p supercapacitor. This kind of supercapacitor is symmetric and consists of two identical p-dopable conducting polymer electrodes. During the charging process, positive electrode is fully p-doped charged and the negative electrode is uncharged.

2. p^a-p^b supercapacitor. This kind of supercapacitor is formed by two different p-dopable conducting polymer electrodes having different potential windows.

3. n-p supercapacitor. This kind of supercapacitor consists of one n-dopable polymer electrode and one p-dopable electrode with the highest potential window among the three structures (~ 3 V).

The conducting polymers used as electrode materials have some drawbacks such as degradation caused by swelling and shrinking during charge-discharge process which leads to worse performance on cycling test. This problem can be mitigated by adding conducting polymers into carbon-based materials to form carbon/conducting polymer composites. These composites combine the advantages of carbon materials and conducting polymers, resulting in better electrochemical performance.

1.4 Challenges and Applications of Supercapacitors

Owing to the unique features and advantages, supercapacitors have been used to deliver power for many applications. They are widely employed in energy storage systems, for example [28, 58-60]:

1. Regenerative braking system in electrical vehicles.
2. Burst-power generation system in electronic devices.
3. Actuation systems in space vehicles.
4. Dynamic voltage restorer system to regulate voltage for the electricity grid.
5. Loading and unloading system in gantry cranes.
6. Back-up power systems for memories, adjustable speed drives and power electronics.

Although supercapacitors have a lot of industrial, commercial and military applications, low energy density is still an intrinsic drawback for supercapacitors. To overcome this problem, new energy-storage materials should be developed to increase the capacitance and operating voltage of supercapacitors for achieving higher energy density without scarifying cycling stability and power density.

1.5 Research Objectives and Outline

In recent years, due to the rapid developments in portable and flexible electronic equipment, there is a great demand for high-performance and flexible power sources. Supercapacitors have fast charging-discharging rate, high power

density, and extremely long cycle life, making them very promising energy storage devices for electronic systems. Many researches on supercapacitors have been conducted. A lot of materials have been used to fabricate supercapacitors such as carbon based materials and faradaic materials. However, many of the existing materials have low energy density which is the major obstacle to fully replace batteries in many energy storage applications. The performance of a supercapacitor depends greatly on three parameters: (1) capacitance, (2) operating voltage, and (3) equivalent inner resistance, which are strongly influenced by the physical and chemical properties of the electrode materials, electrolytes and electrode configurations. Hence, the main aim of this research work is to develop suitable electrode materials and structures for supercapacitors with excellent electrochemical characteristics such as high capacitance, long cycle life, high flexibility, fast charge/discharge rate, high energy density and high power density for energy storage.

The organization of this thesis is as follows. In Chapter 2, the electrochemical properties of solid-state supercapacitors based on $MnCo_2S_4$@$NiCo(OH)_2$ core-shell nanocomposite are studied. The effect of $NiCo(OH)_2$ on the supercapacitor performance is discussed. Chapter 3 compares the physical and electrochemical characteristics of three electrode materials: $MnCo_2O_4$, $MnCo_2S_4$ and $MnCo_2S_4$@Ni-Co-S with the help of scanning electron microscopy, transmission electron microscopy, accelerated surface area and porosimetry system, x-ray diffraction and electrochemical workstation. The electrical properties of an asymmetric

supercapacitor based on $MnCo_2S_4$@Ni-Co-S and activated carbon on Ni foam are also investigated. In Chapter 4, a flexible solid-state supercapacitor based on CNTs and Ni-Co-S on papers is characterized and compared with its counterpart without Ni-Co-S. Chapter 5 introduces the solid-state flexible supercapacitor based on inkjet printed interdigitated electrodes. The influences of the dimensions of the interdigitated electrodes on the electrochemical properties of the supercapacitors are presented. Chapter 6 summarizes the main results obtained in this research.

1.6 References

[1] J. R. Miller, P. Simon, *Science*, 2008, **321**, 651.

[2] V. V. N. Obreja, *Phys*. *E*., 2008, **40**, 2596–2605.

[3] W. Yang, M. Ni, X. Ren, Y. Tian, N. LI, Y. Su, X. Zhang, *Current Opinion in Colloid & Interface Science*, 2015, **20**, 416.

[4] S. Kandalkar, D. Dhawale, C. Kim, C. Lokhande, *Synth*. *Met*., 2010, **160**, 1299.

[5] R. Kötz, S. Müller, M. Bärtschi, B. Schnyder, P. Dietrich, F. N. Büchi, A. Tsukada, G. G. Scherer, P. Rodatz, O. Garcia, P. Barrade, V. Hermann, R. Gallay, *Electrochem*. *Soc*. *Proc*., 2001, **21**, 564.

[6] A. G. Pandolfo, A. Hollenkamp, *J*. *Power Sources*, 2006, **157**, 11.

[7] P. Sharma, T. S. Bhatti, Energy Convers. *Manage*., 2010, **51**, 2901.

[8] G. P. Wang, L. Zhang, J. J. Zhang, Chem. *Soc*. *Rev*., 2012, **41**, 797–828.

[9] L. Zhang, X. S. Zhao, Chem. *Soc*. *Rev*., 2009, **38**, 2520

[10] R. Kotz, M. Carlen, *Electrochimica Acta*, 2000, **45**, 2483.

[11] M. Endo, T. Takeda, Y. J. Kim, K. Koshiba, K. Ishiii, *Carbon Sci*., 2000, **1**, 91.

[12] E. Raymundo-Pinero, K. Kierzek, J. Machnikowski, F. Beguin, *Carbon*, 2006, **44**, 2498.

[13] B.E. Conway, *J*. *Solid State Electrochem*, 2003, **7**, 637.

[14] P. Simon, Y. Gogotsi, *Nat Mater* 2008, **7**, 845.

[15] W. Wei, X. Cui, W. Chen, D.G. Ivey, *Chem Soc Rev*, 2011, **40**, 1697.

[16] A. Gonzalez, E. Goikolea, J.A. Barrena, R. Mysyk, *Renewable and Sustainable Energy Review*, 2016, **56**, 1189.

[17] H. Shi, *Electrochim*. *Acta*, 1996, **41**, 1633.

[18] D. Qu, H. Shi, *J*. *Power Sources*, 1998, **74**, 99.

[19] R. B. Rakhi, W. Chen, D. K. Cha, H. N. Alshareef, *Nano Lett*., 2012, **12**, 2559–2567.

[20] M. Lee, G.-P. Kim, H.D. Song, S. Park, J. Yi, *Nanotechnology*, 2014, **25**, 345601.

[21] C. Chen, Y. Zhang, Y. Li, J. Dai, J. Song, Y. Yao, Y. Gong, I. Kierzewski, J. Xie, L. Hu, *Energy Environ*. *Sci*., 2017, **10**, 538–545.

[22] J. Mi, X.R. Wang, R.J. Fan, W.H. Qu, W.C. Li, *Energy Fuels*, 2012, **26**,531.

[23] L. Wei, M. Sevilla, A.B. Fuertes, R. Mokaya, G. Yushin, *Adv*. *Energy Mater*., 2011, **1**, 356.

[24] F.C. Wu, R.L. Tseng, C.C. Hu, C.C. Wang, *J*. *Power Sources*, 2005, **144**, 302.

[25] J. Yan, Q. Wang, T. Wei, Z. Fan, *Adv*. *Energy Mater*., 2014, **4**, 1300816.

[26] M. Endo, T. Maeda, T. Takeda, Y. J. Kim, K. Koshiba, H. Hara, M. S. Dresselhaus, *J*. *Electrochem*. *Soc*., 2001, **148**, A910.

[27] E. Frackowiak, *Phys*. *Chem*. *Chem*. *Phys*., 2007, **9**, 1774.

[28] B.E. Conway, *Electrochemical Capacitor, Scientific, Fundamentals and Technological Applications*, Plenum Press, New York, 1999, p. 105.

[29] K. Kierzek, E. Frackowiak, G. Lota, G. Gryglewicz, J. Machnikowski, *Electrochim*. *Acta*, 2004, **49**, 515.

[30] G. Salitra, A. Soffer, L. Eliad, Y. Cohen, D. Aurbach, *J*. *Electrochem*. *Soc*., 2000, **147**, 2486.

[31] Y. Marcus, *Chem*. *Rev*., 1988, **88**, 1475.

[32] C. Largeot, C. Portet, J. Chmiola, P.L. Taberna, Y. Gogotsi, P. Simon, *J*. *Am*. *Chem*. *Soc*., 2008, **130**, 2730.

[33] D. N. Futaba, K. Hata, T. Yamada, T. Hiraoka, Y. Hayamizu, Y. Kakudate, O. Tanaike, H. Hatori, M. Yumura, S. Iijima, *Nat*. *Mater*., 2006, **5**, 987.

[34] K.H. An, K.K. Jeon, W.S. Kim, Y.S. Park, S.C. Lim, D.J. Bae, Y.H. Lee, *J*. *Korean Physical Society*, 2001, **39**, S511.

[35] W. Lu, L. Qu, K. Henry, L. Dai, *J*. *of Power Sources*, 2009, **189**, 1270.

[36] L. Z. Fan, Y. S. Hu, J. Maier, P. Adelhelm, B. Smarsly, M. Antonietti, *Adv*. *Funct*. *Mater*., 2007, **17**, 3083.

[37] W. Fan, C. Zhang, W.W. Tjiu, K. P. Pramoda, C. He, T. Liu, *Applied Materials & Interface*, 2013, **5**, 3382.

[38] Z. Bo, W. Zhu, W. Ma, Z. Wen, X. Shuai, J. Chen, J. Yan, Z. Wang, K. Cen, X. Feng, *Advanced Materials*, 2013, **25**, 5779.

[39] Y. Xu, K. Sheng, C. Li, G. Shi, *ACS Nano*, 2010, **4**, 4324.

[40] H.C. Huang, C.W. Huang, C.T. Hsieh, P.L. Kuo, J.M. Ting, H. Teng, *J. Phys. Chem. C*, 2011, **115**, 20689.

[41] Y. Zhu, S. Murali, M.D. Stoller, A. Velamakanni, R.D. Piner, R.S. Ruoff, *Carbon*, 2010, **48**, 2118.

[42] C. Liu, Z. Yu, D. Neff, A. Zhamu, B.Z. Jang, *Nano Letters*, 2010, **10**, 4863.

[43] Z.S. Wu, G. Zhou, L.C. Yin, W. Ren, F. LI, H.M. Cheng, *Nano Energy*, 2012, **1**, 107.

[44] C.-C. Hu, C.-C. Wang, *J. Power Sources,* 2004, **125**, 299.

[45] B.L. Ellis, P. Knauth, T. Djenizian, *Advanced Materials*, 2014, **26**, 3368.

[46] S. Trasatti, *Electrochim. Acta*, 1991, 36, 225.

[47] V. D. Patake, C. D. Lokhande, O. S. Joo, *Appl. Surf. Sci*., 2009, **255**, 4192.

[48] N.L. Wu, S.L. Kuo, M.H. Lee, *J. of Power Sources*, 2001, **104**, 62.

[49] J. P. Zheng, J. Huang, T. R. Jow, *J. Electrochem. Soc*., 1997, **144**, 2026.

[50] K. R. Prasad, K. Koga, N. Miura, *Chem. Mater*., 2004, **16**, 1845.

[51] M. Kalaji, P. J. Murphy, G. O. Williams, *Synth. Met*., 1999, **102**, 1360.

[52] Y. R. Ahn, M. Y. Song, S. M. Jo, C. R. Park, *Nanotechnology*, 2006, **17**, 2865.

[53] M. Toupin, T. Brousse, D. Bélanger, *Chem*. *Mater*., 2004, **16**, 3184.

[54] V. Gupta, N. Miura, Mater. *Lett*., 2006, **60**, 1466.

[55] B. Fang, L. Binder, *J*. *Power Sources*, 2006, **163**, 616.

[56] S. A. Hashmi, H. M. Upadhyaya, *Solid State Ionics*, 2002, **152**, 883.

[57] A. Rudge, J. Davey, I. Raistrick, S. Gottesfeld, J.P. Ferraris, *J*. *of Power Sources*, 1994, **47**, 89.

[58] A. Yu, V. Chabot, J. Zhang, *Electrochemical Supercapacitors for Energy Storage and Delivery*, CRC Press, 2013.

[59] J.R. Miller, A. F. Burke, *Interface*, 2008, **17**, 53.

[60] P. Ball, Y. Gogotsi, *Mater Bull*., 2012, **37**, 1000.

Chapter 2

A Study on $MnCo_2S_4$@$NiCo(OH)_2$ Core-Shell Nanocomposite for High-Performance Solid-State Symmetric Applications

2.1 Introduction

As mentioned in Chapter 1, supercapacitors (SCs) with notable features compared to batteries have received extremely high interest from researchers owing to their wide range of applications in portable electronics and electric vehicles [1, 2]. Numerous energy-storage materials such as carbon materials, conducting polymers and metal oxides have been employed to fabricate supercapacitors [3, 4]. Among them, oxides of transition metals have attracted much attention owing to their great flexibility in structure and morphology, large capacity, non-toxicity and low cost [5]. Compared with binary manganese oxide (MnO_2) and cobalt oxide (Co_3O_4), ternary manganese cobalt oxide ($MnCo_2O_4$) demonstrates better electrochemical performance due to the synergistic effect from the two binary metal oxides [6, 7]. However, electrodes based on transition metal oxides have relatively low electrical conductivity and short cycle life [8-12].

Recently, transition metal sulfides, such as CoS [13], NiS [14] and MnS_2 [15] are extensively investigated as a new type of faradaic materials possessing high electrochemical performance for supercapacitors. Particularly, cobalt sulfide which

could transfer to different phases for example $Co_{1-x}S$, CoS_2, Co_9S_8 and Co_3S_4 exhibits multiple oxidation states and shows high pseudo-capacitance. The addition of sulfur into the transition metal oxides could lower the internal resistance to enhance the charge transport and charge-collection ability, thus increasing the capacitance of the electrode material, hence the energy density and power density for many high-power applications. Ternary transition metal sulfides such as $NiCo_2S_4$ and $MnCo_2S_4$ produced by mixing two metal sulfides show higher electrochemical activity than the binary metal sulfides like NiS_x [16], MnS_x [17] and CoS_x [18]. In comparison to their oxide counterparts, the ternary metal sulfides demonstrate higher conductivity and smaller optical band gap [19-23]. The low electronegativity of sulphur in sulphospinel could also avoid severe structural expansion and thus enhance the mechanical stability [24]. In addition, the co-existence of two pseudocapacitive materials in the ternary transition metal sulfides could increase the reduction-oxidation reactions and hence offer a higher capacitance [25].

Moreover, the electrode structure could influence the electrochemical performance of a supercapacitor. Core-shell structure is regarded as a promising electrode configuration owing to its rich redox reaction sites and sufficient contact area between electrode and electrolyte. By the synergistic effect of core and shell materials, the performance of the core-shell hybrid electrode could be greatly enhanced [26-28]. In this Chapter, a ternary metal sulphide nanostructure $MnCo_2S_4$ is fabricated to combine the advantages of CoS_x and MnS_x for supercapacitors. To

further improve the electrochemical characteristics, Ni-Co hydroxide nanosheet is coated on the surface of $MnCo_2S_4$ to form a hierarchical core-shell structure $MnCo_2S_4$@$NiCo(OH)_2$ (MCS@NCOH). The $MnCo_2S_4$ nanorods not only exhibit excellent electrochemical behavior by themselves, but also employ as effective frameworks to load additional electroactive material for increasing the capacitance of the electrode. After the deposition of $NiCo(OH)_2$ nanosheet on Ni foam-$MnCo_2S_4$ electrode, the mechanical stability of the whole electrode is strengthened with larger electroactive surface area, good electrical conductivity and richer reduction-oxidation reaction sites to facilitate ion diffusion and charge transport, leading to higher charge storage capacity.

2.2 Experimental

2.2.1 Synthesis of $MnCo_2S_4$ Nanorods

$MnCo_2O_4$ nanorods were prepared by a hydrothermal process. Nickel foam substrates with the size of 15 mm×30 mm×1 mm were cleaned with acetone, diluted hydrochloric acid and ethyl alcohol successively with ultrasound. $MnCl_2 \cdot 4\ H_2O$ (1 mmol), $CoCl_2 \cdot 4\ H_2O$ (2 mmol), urea (10 mmol) and hexamethylenetetramine (HMTA) (2 mmol) were dissolved in deionized (DI) water (40 mL) with vigorous stirring to obtain a pink solution. This pink solution and the Ni foam were then transferred into a Teflon lined stainless steel autoclave (45 mL). To obtain the Mn-Co precursors, the autoclave was heated at 95 ^{o}C in an oven for 6 hours. After cooling down to room

temperature, the sample (Ni foam with loaded precursors) was rinsed with ethanol and DI water. It was then dried at 60 ^{o}C. After an annealing treatment at 300 ^{o}C for two hours in air, $MnCo_2O_4$ on Ni foam was obtained. The Ni foam with as-deposited $MnCo_2O_4$ was then immersed in a solution prepared by mixing $Na_2S{\cdot}12H_2O$ (5 mmol) and DI water (40 mL) in an autoclave at 90 ^{o}C for 10 hours. This process is called sulfurization in which $MnCo_2O_4$ was converted to $MnCo_2S_4$.

2.2.2 Preparation of $MnCo_2S_4$@$NiCo(OH)_2$ Hybrid Structure

The $MnCo_2S_4$ supported by Ni foam acted as a skeleton for the growth of Ni-Co hydroxide through a simple electrochemical deposition method. Firstly, an aqueous electrolyte was made by dissolving $Ni(NO_3)_2H_2O$ (7.5 mM) and $Co(NO_3)_2H_2O$ (7.5 mM) in 50 mL of DI water. Then, a typical three-electrode configuration was employed to perform the deposition process with the Ni foam-MCS as the working electrode, a platinum foil as counter electrode and an Ag/AgCl as reference electrode. By applying a potential between -1.2 V and 0.2 V with a scan rate of 10 mV/s for 6 cycles, the deposition was conducted. Figure 2.1 shows the schematic diagram of the fabrication procedure of the core-shell hybrid electrode.

2.2.3 Fabrication of Solid-State Symmetric Supercapacitor

The polyvinyl alcohol (PVA)/KOH solid-state gel electrolyte was first prepared by mixing KOH (5.2 g) and PVA (5.6 g) into DI water (50 mL) with stirring

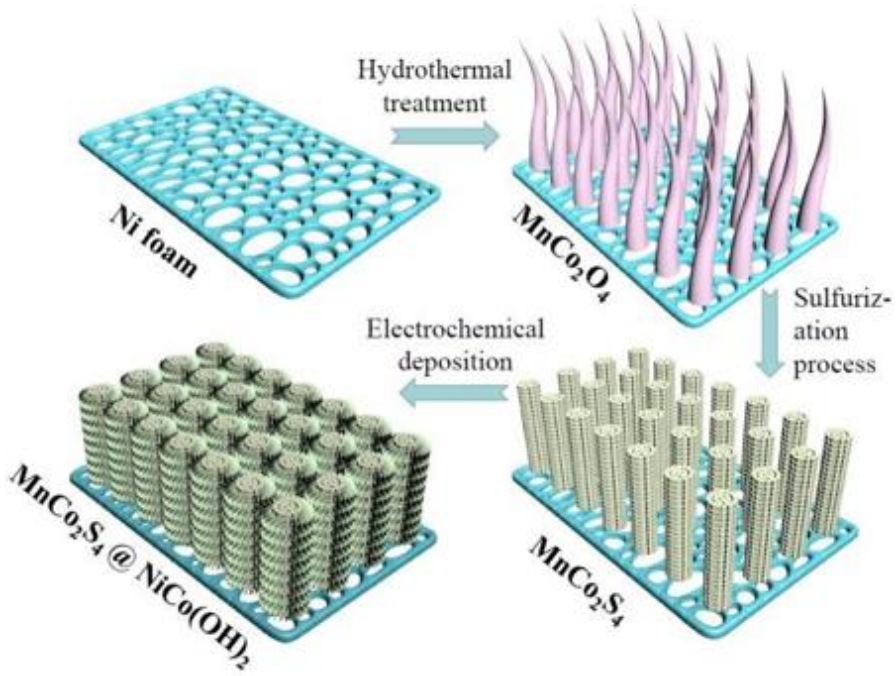

Figure 2.1. Schematic diagram of the fabrication procedure of the MCS@NCOH core-shell hybrid electrode.

at 80 ^{o}C for 4 hours. Two pieces of MCS@NCOH-coated Ni foam substrate were then soaked in the PVA/KOH gel for 3 minutes and sandwiched with a thin insulating plate as a separator to form a supercapacitor. For the sake of comparison, a supercapacitor based on Ni foam-MCS electrode was also fabricated.

2.3 Results and Discussion

The electrochemical measurements of the Ni foam@MCS and Ni foam@MCS@NCOH core-shell electrodes were conducted using a three-electrode cell in 3 M KOH. The cyclic voltammetry (CV) curves of the electrodes at a scan rate of 10 mV/s are shown in Figure 2.2a. The CV curve of both electrodes has redox

peaks. These peaks should be due to the reversible reduction-oxidation reactions of the active materials. It is found that the CV area of the Ni foam@MCS@NCOH electrode is larger than that of the Ni foam@MCS electrode. This implies that NCOH can enhance the charge storage capacity. Figure 2.2b depicts the CV curves of Ni foam@MCS@NCOH at different scan rates. With increasing scan rate, the cathodic peak shifts to positive potential and the anodic peak shifts to negative potential. This implies that the core-shell electrode has good stability of capacitance at high charge/discharge rate [29]. Figure 2.2c shows the galvanostatic discharge curves of

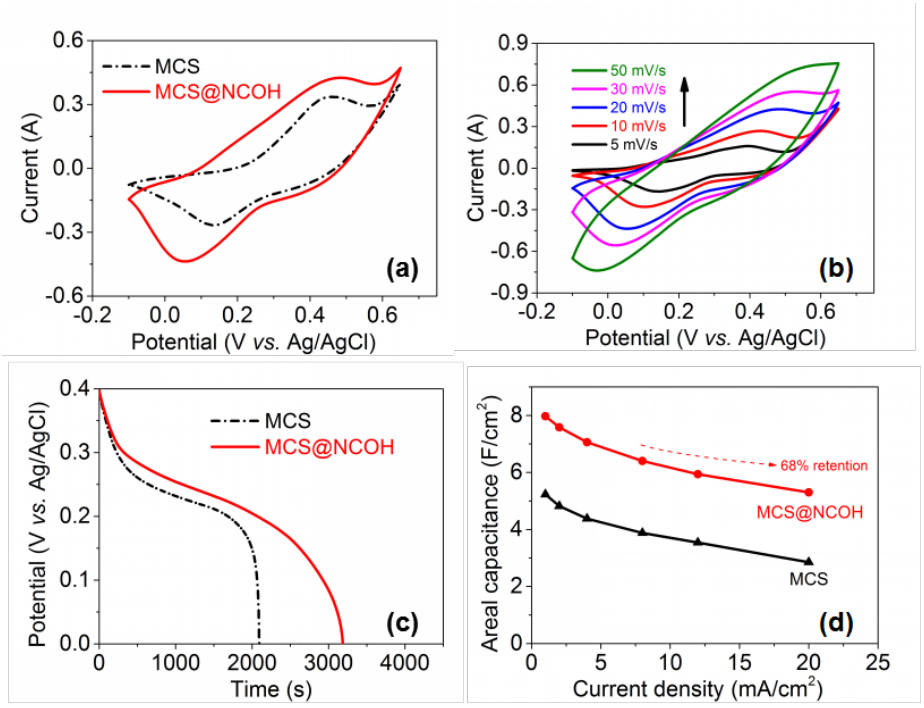

Figure 2.2. (a) CV curves of Ni foam@MCS and Ni foam@MCS@NCOH electrodes at the scan rate of 10 mV/s. (b) CV curves of the Ni foam@MCS@NCOH electrode measured at different scan rates. (c) Galvanostatic discharge curve of the Ni foam@MCS and Ni foam@MCS@NCOH electrodes. (d) Comparison of areal capacitance of Ni foam@MCS and Ni foam@MCS@NCOH electrodes.

the Ni foam@MCS and Ni foam@MCS@NCOH electrodes at a current density of 1 mA/cm^2. The plateau in the discharge curves reveals the pseudocapacitive properties of the electrode materials [29]. From Figure 2.2c, it can be noticed that the electrode-potential (IR) drop of the MCS@NCOH sample is smaller than that of the MCS sample, indicating that the MCS@NCOH core-shell structure has lower electrode and transport resistance. The areal capacitance C_a of an electrode could be calculated from the discharge curve based on the following equation:

$$C_a = (I\Delta t)/(S\Delta V) \tag{2.1}$$

where S is the area of the electrode, I the discharge current, Δt the discharge time and ΔV the potential window. Figure 2.2d shows a plot of areal capacitance of the electrodes versus current density. At a current density of 1 mA/cm^2, the Ni foam@MCS@NCOH electrode has a capacitance of 7.97 F/cm^2 which is 1.5 times larger than its counterpart without NCOH. After increasing the current density 20 times, the Ni foam@MCS@NCOH electrode can keep 68 % of the initial capacitance (5.3 F/cm^2), indicating a good rate capability. It has been reported that the addition of NCOH can effectively enhance the cycling stability of the electrode [30].

A solid-state symmetric SC using Ni foam@MCS@NCOH as both positive and negative electrodes was then fabricated in order to further exhibit the capacitive behavior of the core-shell $MnCo_2S_4$-$NiCo(OH)_2$ nanocomposite. Figure 2.3a depicts the cycle voltammetry curves of the SC based on Ni foam@MCS@NCOH at various scan rates (5, 10, 20, 30 and 50 mV/s) in a potential window of -0.1 – 0.65 V. The

CV profiles keep similar shape as the scan rate increases. This indicates a good capacitive behavior. Figure 2.3b shows the galvanostatic charge/discharge (GCD) curves of the symmetric SC based on Ni foam@MCS@NCOH at various current densities (1, 2, 4, 8, 12, 20 mA/cm^2). At a current density of 1 mA/cm^2, the capacitance of the Ni foam@MCS@NCOH-based SC device is 4.5 times larger than its counterpart based on Ni foam@MCS (Figure 2.3c). The relationship between the

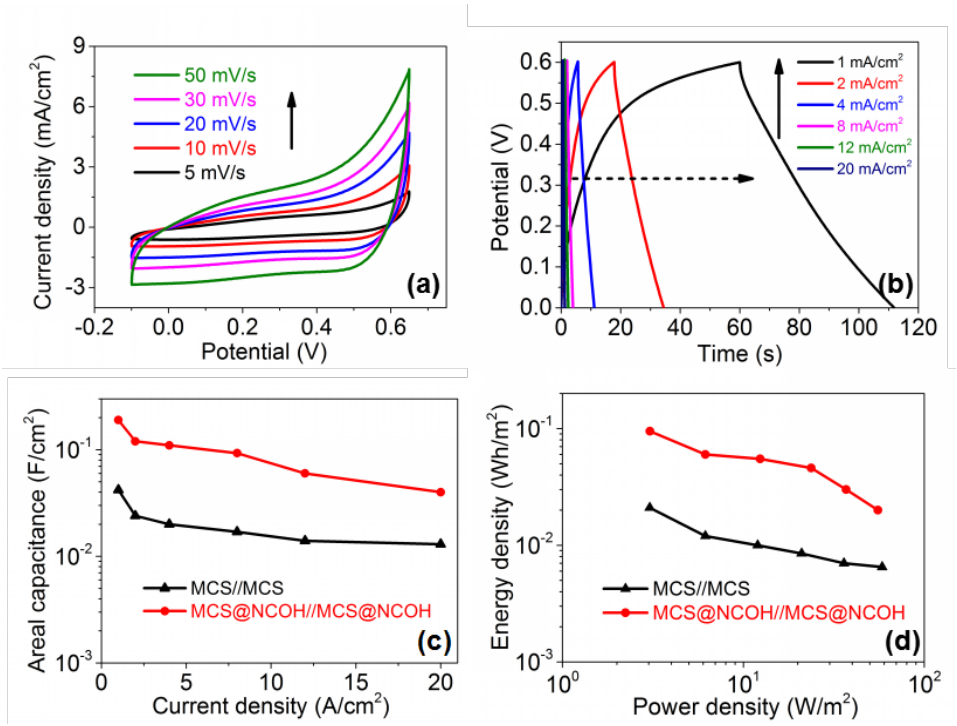

Figure 2.3. (a) CV curves of MCS@NCOH//MCS@NCOH symmetric SC on Ni foam. (b) GCD curves of symmetric SC made by Ni foam@MCS@NCOH hybrid electrodes. (c) Areal capacitance as a function of current density for the MCS//MCS and MCS@NCOH//MCS@NCOH SCs. (d) Ragone plots of the studied SCs.

areal energy density and the power density (the Ragone plot) is shown in Figure 2.3d. The energy density E_a and the power density P_a could be calculated according to the following equations:

$$E_a = 0.5C_a^{'}U^2 \tag{2.2}$$

$$P_a = E_a/\Delta t \tag{2.3}$$

where $C_a^{'}$ is the areal capacitance of the SC device and U is the cell voltage.

The maximum energy density of the Ni foam@MCS@NCOH-based SC is 95 mWh/m^2 which is 350 % higher than that of its counterpart based on Ni foam@MCS. The high performance of the Ni foam@MCS@NCOH-based supercapacitor could be attributed to the following reasons: (1) the core-shell hybrid structure increases the interfacial area between the electrode and the electrolyte, thus enabling effective electrolyte transport and electroactive-site accessibility; (2) the Ni-Co hydroxide (shell material) combining the advantages of nickel hydroxide and cobalt hydroxide can improve the faradaic reduction-oxidation reactions and thus the pseudocapacitance; and (3) the manganese cobalt sulfide (core material) has high conductivity, leading to good rate capability.

2.4 Summary

In summary, $NiCo(OH)_2$ nanosheets were coated on the $MnCo_2S_4$ surface by a simple electrochemical deposition method to form a core-shell nanostructure

$MnCo_2S_4$@$NiCo(OH)_2$ on the nickel foam substrate. The electrode with as-fabricated core-shell nanostructure demonstrates excellent areal capacitance of 7.97 F/cm^2 at 1 mA/cm^2. Owing to the synergistic effect from $MnCo_2S_4$ and $NiCo(OH)_2$, the symmetric SC fabricated using this core-shell hybrid electrode and solid-state electrolyte exhibits good electrochemical performance, indicating its great potential applications as an energy storage component.

2.5 References

[1] M. F. El-Kady, V. Strong, S. Dubin, R.B. Kaner, *Science*, 2012 **335**, 1326.

[2] L.L. Zhang, X.S. Zhao, *Chemical Society Reviews*, 2009, **38**, 2520.

[3] L. Wei, M. Sevilla, A. B. Fuertes, R. Mokaya, G. Yushin, *Advanced Energy Materials*, 2011, **1**, 356.

[4] P. Yang, Y. Ding, Z. Lin, Z. Chen, Y. Li, P. Qiang, M. Ebrahimi, W. Mai, C.P. Wong, Z.L. Wang, *Nano Letters*, 2014, **14**, 731.

[5] S. Wang, B. Pei, X. Zhao, R. A. Dryfe, *Nano Energy* **2013**, 2, 530.

[6] Y. Xu, X. Wang, C. An, Y. Wang, L. Jiao, H. Yuan, *J*. *Mater*. *Chem*. *A* **2014**, 2, 16480.

[7] L. Li, Y. Q. Zhang, X. Y. Liu, S. J. Shi, X. Y. Zhao, H. Zhang, X. Ge, G. F. Cai, C.D. Gu, X. L. Wang, J. P. Tu. *Electrochim*. *Acta* **2014**, 116, 467.

[8] H. Chen, J. Jiang, L. Zhang, H. Wan, T. Qi, D. Xia, *Nanoscale* **2013**, 5, 8879.

[9] S. Tang, B. Zhu, X. Shi, J. Wu, X. Meng, *Adv*. *Energy Mater*. **2017**, 7, 1601985.

[10] W. Du, Y. Gao, Q. Tian, D. Li, Z. Zhang, J. Guo, X. Qian, *J*. *Nanopart*. *Res*. **2015**, 17, 368.

[11] C. Yuan, J. Li, L. Hou, X. Zhang, L. Shen, X. W. D. Lou, *Adv*. *Funct*. *Mater*. **2012**, 22, 4592.

[12] Z. Lu, Z. Chang, J. Liu, X. Sun, *Nano Res*. **2011**, 4, 658.

[13] X. Xia, C. Zhu, J. Luo, Z. Zeng, C. Guan, C. F. Ng, H. Zhang, H. J. Fan, *Small* **2014**, 10, 766.

[14] J. Yang, X. Duan, Q. Qin, W. Zheng, *J*. *Mater*. *Chem*. *A* **2013**, 1, 7880.

[15] G. Ma, H. Peng, J. Mu, H. Huang, X. Zhou, Z. Lei, *J*. *Power Sources* **2013**, 229, 72.

[16] X. Y. Yu, L. Yu, L. Shen, X. Song, H. Chen, X. W. D. Lou, *Adv*. *Funct*. *Mater*. **2014**, 24, 7440.

[17] Y. Tang, T. Chen, S. Yu, Y. Qiao, S. Mu, J. Hu, F. Gao, *J*. *Mater*. Chem. A 2015, 3, 12913.

[18] S. Peng, L. Li, H. Tan, R. Cai, W. Shi, C. Li, S. G. Mhaisalkar, M. Srinivasan, S. Ramakrishna, Q. Yan, *Adv*. *Funct*. *Mater*., 2014, **24**, 2155.

[19] H. Chen, J. Jiang, L. Zhang, D. Xia, Y. Zhao, D. Guo, T. Qi, H. Wan, *J*. *Power Sources*, 2014, **254**, 249.

[20] Y. Tao, L. Ruiyi, L. Zaijun, *Mater*. *Lett*., 2016, 167, 234.

[21] L. Mei, T. Yang, C. Xu, M. Zhang, L. Chen, Q. Li, T. Wang, *Nano Energy*, 2014, **3**, 36.

[22] L. Shen, J. Wang, G. Xu, H. Li, H. Dou, X. Zhang, *Adv*. *Energy Mater*., 2015, **5**, 1400977.

[23] J. Xiao, L. Wan, S. Yang, F. Xiao, S. Wang, *Nano Lett*.,2014, **14**, 831.

[24] Y. Zhu, X. Ji, Z. Wu, Y. Liu, *Electrochim*. *Acta*, 2015, **186**, 562.

[25] Y. M. Chen, Z. Li, X. W. D. Lou, *Angew*. *Chem*., 2015, **127**, 10667.

[26] J. Yang, M. Ma, C. Sun, Y. Zhang, W. Huang, X. Dong, *J*. *Mater*. *Chem*. *A*, 2015, **3**, 1258.

[27] W. Fu, C. Zhao, W. Han, Y. Liu, H. Zhao, Y. Ma, E. Xie, *J*. *Mater*. *Chem*. *A*, 2015, **3**, 10492.

[28] R. Li, S. Wang, Z. Huang, F. Lu, T. He, *J*. *Power Sources*, 2016, **312**, 156.

[29] W. Fu, Y. Wang, W. Han, Z. Zhang, H. Zha, E. Xie, *Journal of Materials Chemistry A*, 2016, **4**, 173.

[30] W. Zhou, K. Yu, D.Wang, J. Chu, J. Li, L. Zhao, C. Ding, Y. Du, X. Jia, H. Wang, G. Wen, *Nanotechnology*, 2016, **27**, 235402.

Chapter 3

Double-Layer $MnCo_2S_4$@Ni-Co-S Core/Shell Nanostructure on Nickel Foam for High-Performance Supercapacitor

3.1 Introduction

In this Chapter, with the intention of promoting the electrochemical performance, a ternary metal sulphide Ni-Co-S nanosheet is coated on the surface of $MnCo_2S_4$ by a simple electrochemical deposition to form a $MnCo_2S_4$@Ni-Co-S (MCS@NCS) core-shell nanostructure on nickel foam. Physical measurements such as scanning electron microscopy, transmission electron microscopy and x-ray diffraction as well as electrochemical measurements are performed to study the morphology and electrochemical behavior of the electrode. For the purpose of comparison, electrodes based on $MnCo_2O_4$ and $MnCo_2S_4$ are also fabricated and characterized. In addition, an asymmetric supercapacitor (ASC) using Ni foam@MCS@NCS as the positive electrode and Ni foam@activated carbon as the negative electrode are prepared with KOH as the electrolyte. The fabricated ASC demonstrates remarkable capacitance and durability, revealing its great potential as an energy storage device.

3.2 Experimental

3.2.1 Fabrication of $MnCo_2O_4$ Nanorods

A hydrothermal process was used to synthesize $MnCo_2O_4$ (MCO) nanorods. Nickel foam was first cut into pieces with the dimension of 15 mm×30 mm×1 mm. It was then ultrasonically cleaned with acetone, diluted hydrochloric acid and ethyl alcohol successively. To facilitate subsequent electrochemical measurement by an electrochemical workstation, ~10 mm×10 mm Ni foam was protected by polytetrafluoroethylene tape to avoid the Ni foam contacting with solution during fabrication. A pink solution was then prepared by dissolving $MnCl_2 \cdot 4H_2O$ (1 mmol), $CoCl_2 \cdot 6H_2O$ (2 mmol), urea (10 mmol) and hexamethylenetetramine (HMTA) (2 mmol) in deionized water (40 mL) with vigorous stirring. After that, the precleared nickel foam and the as-prepared pink solution were put into a Teflon lined stainless steel autoclave (45 mL). In order to obtain the Mn-Co precursors, the autoclave was then heated at 95 ^oC for 6 hours in an oven. After cooling down to room temperature, the nickel foam with loaded precursors was cleaned with ethanol and later dried at 60 ^oC. $MnCo_2O_4$ on Ni foam was synthesized after undergoing an annealing in air at 200 ^oC for 2 hours.

3.2.2 Synthesis of $MnCo_2S_4$ Nanorods

A sulfurization process was utilized to obtain the $MnCo_2S_4$ nanorods. The nickel foam with as-grown $MnCo_2O_4$ was immersed in a solution formed by mixing

$Na_2S \cdot 9H_2O$ (5 mmol) and deionized water (40 mL) in an autoclave at 90 ^oC for 10 hours, followed by rinsing with ethanol and drying at 60 ^oC.

3.2.3 Preparation of the $MnCo_2S_4$@Ni-Co-S Hybrid Electrode

The $MnCo_2S_4$ on nickel foam acted as a scaffold for the growth of Ni-Co-S via a simple electrochemical deposition method. A pink solution was first prepared by dissolving $Ni(NO_3)_2 \cdot 6H_2O$ (7.5 mM), $Co(NO_3)_2 \cdot 6H_2O$ (7.5 mM) and thiourea (75 mM) in 50 mL of deionized water. A Ni-Co-S nanosheet was then coated on the surface of $MnCo_2S_4$ nanorods by applying a potential between -1.2 V and 0.2 V with the scan rate of 10 mV/s for 6 cycles in an electrochemical system. The pink solution was used as an aqueous electrolyte in the deposition process. The electrode was then rinsed with ethanol and dried.

3.2.4 Assembly of the Asymmetric Supercapacitor

An asymmetric supercapacitor was fabricated by assembling the MCS@NCS-coated Ni foam (positive electrode), the activated carbon (AC)-coated Ni foam (negative electrode) and a piece of cellulose (separator) together. A traditional slurry coating method was used to prepare the activated carbon. Firstly, activated carbon powders (80 wt%), acetylene black (10 wt%) and polytetrafluoroethylene (10 wt%) were mixed together. Then, the mixture was pressed onto the nickel foam covering an area of 15 mm×20 mm and dried overnight.

3.2.5 Materials Characterization

Field-emission scanning electron microscopy (FE-SEM, JEOL, SM-31010, Japan), transmission electron microscopy (TEM, Hitachi, Japan, HT 7700), x-ray diffraction (XRD, Rigaku SmartLab), and accelerated surface area and porosimetry system (Micromeritics ASAP 2010) were used to characterize the samples.

3.2.6 Electrochemical Measurement

All the electrochemical measurements were performed by a Solarton electrochemical workstation with 3 M KOH as the electrolyte. In half-cell tests, a typical three-electrode system was employed with the as-prepared electrode material on nickel foam as the working electrode, a platinum sheet as the counter electrode and a saturated Ag/AgCl electrode as the reference electrode. The areal capacitance of the electrode was calculated from the galvanostatic charge-discharge (GCD) curves.

In order to maximize the capacitance for the ASC, the charge (q) stored by the positive electrode and the negative electrode need to be carefully balanced. The mass ratio of the electrodes could be calculated by the following equations:

$$q = C_m \Delta V m \tag{3.1}$$

$$q^+ = q^- \tag{3.2}$$

$$\frac{m^+}{m^-} = \frac{C_m^- \Delta V^-}{C_m^+ \Delta V^+} \tag{3.3}$$

where C_m is the specific capacitance of an electrode, m the mass of the active materials of an electrode and the superscripts "+" and "-" represent the positive and

negative electrodes respectively.

The areal energy density (E_a) and power density (P_a) of the ASC could be calculated based on the following equations:

$$E_a = 0.5CU^2 / a \tag{3.4}$$

$$P_a = E_a / \Delta t \tag{3.5}$$

where U is the operating window of the asymmetric supercapacitor, C the capacitance of asymmetric supercapacitor device and a the area of the device.

The gravimetric energy density (E_g) and power density (P_g) of the ASC could be calculated from equation (3.6) and (3.7) respectively.

$$E_g = 0.5CU^2 / m \tag{3.6}$$

$$P_g = E_g / \Delta t \tag{3.7}$$

where m is the total mass of the active materials in the device.

3.3 Results and Discussion

The fabrication process of the $MnCo_2S_4$@Ni-Co-S core-shell nanostructure grown on nickel foam through a simple synthetic method is illustrated in Figure 3.1. First, Mn^{2+} and Co^{2+} ions in alkali solution form the MnCo-layered double hydroxide (LDH) [1] using HMTA as a structure-director and the $MnCo_2O_4$ precursor was obtained after annealing. $MnCo_2O_4$ precursor was then undergone a sulfidation treatment using Na_2S solution, in which $MnCo_2O_4$ precursor experiences a phase

transformation from $MnCo_2O_4$ to $MnCo_2S_4$ nanorods. In this sulfurization process, the Kirkendall effect and volume change occur, causing the formation of corncob-like nanorods [2]. Finally, Ni-Co-S nanosheet was coated on the surface of $MnCo_2S_4$ to form the core-shell structure through a facile electrochemical deposition.

The SEM images of $MnCo_2O_4$, $MnCo_2S_4$ and $MnCo_2S_4$@Ni-Co-S on nickel foam are shown in Figure 3.2a, b and c respectively. Figure 3.2d, e and f show the high resolution TEM images of $MnCo_2O_4$, $MnCo_2S_4$ and $MnCo_2S_4$@Ni-Co-S respectively. As shown in Figure 3.2a and d, the $MnCo_2O_4$ nanorods with diameter of 40-60 nm and needle-like tips are grown on nickel foam. After sulfurization treatment, the needle-like MCS nanorods become corncob-like morphology (Figure 3.2b and e). From the SEM and TEM images, it is obvious that Ni-Co-S nanosheet is

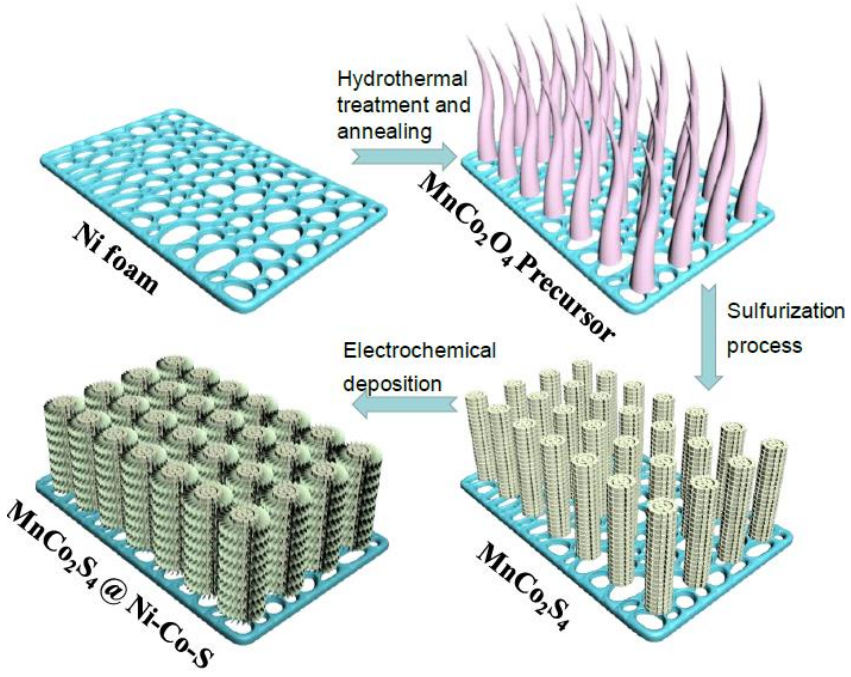

Figure 3.1. A schematic illustration of the fabrication process of the MCS@NCS core-shell nanocomposite on Ni foam.

grown on the $MnCo_2S_4$ nanorods surface uniformly after electrochemical deposition, having highly porous surface (Figure 3.2c and f). The pores can serve as diffusion pathways, enabling sufficient contact with the electrolyte, and thus promote ions transmission and reduction-oxidation reactions in charging and discharging processes [3-5].

The crystal structure of the as-prepared $MnCo_2S_4$, Ni-Co-S and $MnCo_2S_4$@Ni-Co-S was identified by XRD measurement. Figure 3.3a shows the XRD patterns of these core and shell materials. Except for the strong peaks from the nickel foam substrate, the diffraction peaks located at 31.2º, 37.7º, 50º and 55.3º are attributed to the (311), (400), (511) and (440) planes of the $MnCo_2S_4$ respectively, and are similar to those of cubic Co_3S_4 (JCPDS card no. 73-1703), demonstrating that the incorporation of manganese to cobalt sulphide does not alter the crystal structure but

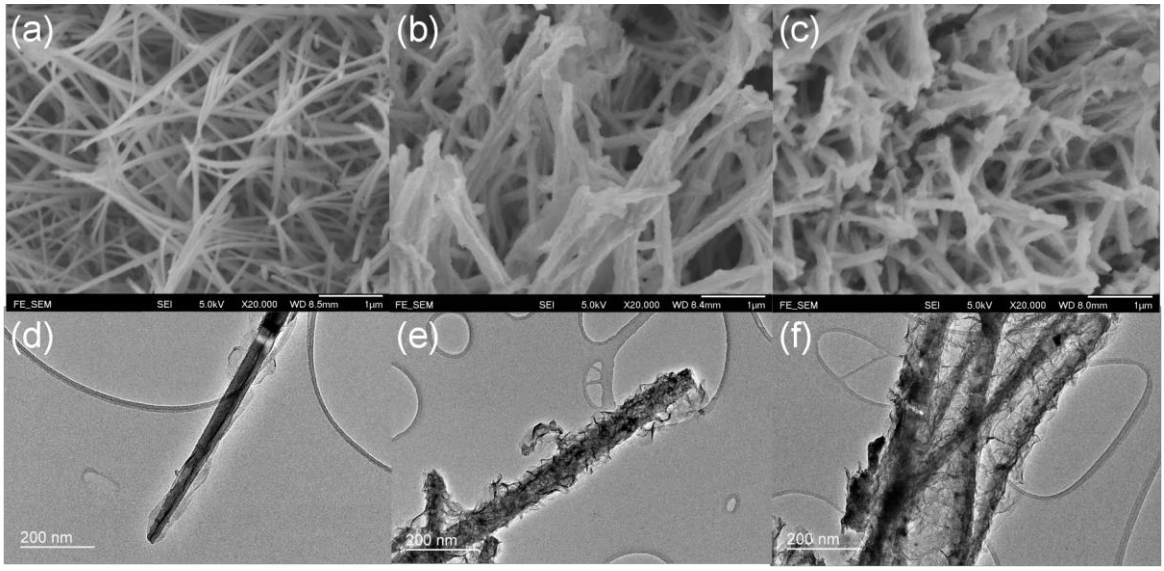

Figure 3.2. SEM images of (a) MCO, (b) MCS and (c) MCS@NCS. TEM images of (d) MCO, (e) MCS and (f) MCS@NCS.

only slightly change the lattice parameters. Due to the low crystallinity of the shell material, no obvious diffraction peak is observed in the XRD pattern of NCS. Moreover, the energy dispersive X-ray (EDX) spectrum reveals that the MCS@NCS core-shell nanocomposite is mainly formed from Mn, Co, Ni and S elements (Figure 3.3b).

Figure 3.4a and b show the N_2 adsorption/desorption isotherms and pore size distribution curves respectively which can be used to investigate the specific surface area and porosity characteristics of the electrode materials. The Brunauer-Emmett-Teller (BET) specific surface area of the MCO, MCS and MCS@NCS is found to be 25.7, 51.1 and 71.3 m^2/g respectively. It is found that the sulfidation process and the hierarchical core-shell structure can greatly increase the specific surface area and hence provide more effective ion transport and active sites for redox reactions. Moreover, the pore size of MCS@NCS is between 2 nm and 10 nm which is a desired porous nature for ions diffusion.

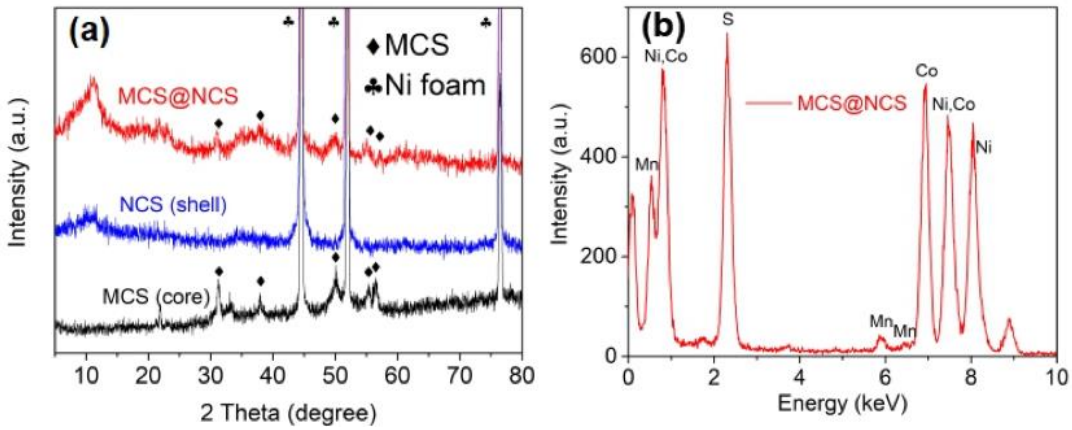

Figure 3.3. (a) XRD patterns of $MnCo_2S_4$, Ni-Co-S and $MnCo_2S_4$@Ni-Co-S. (b) EDX spectrum of the $MnCo_2S_4$@Ni-Co-S core-shell hybrid.

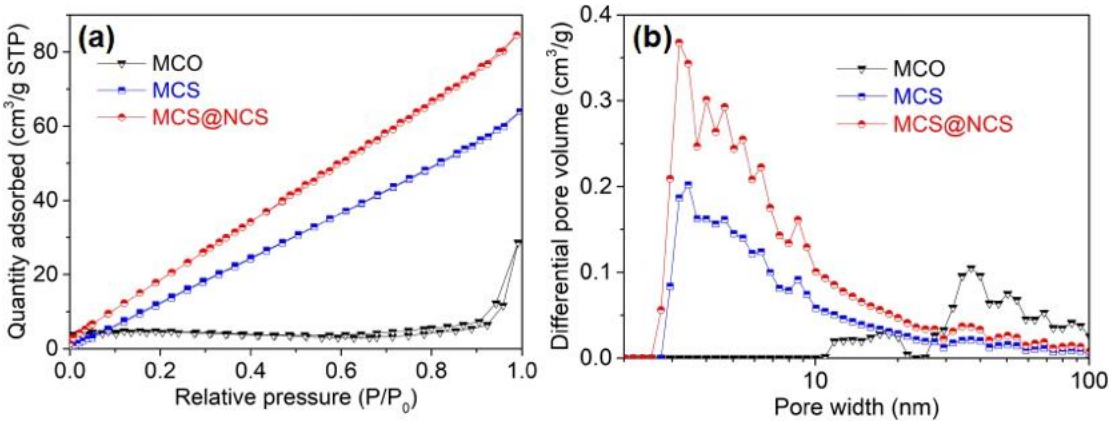

Figure 3.4. (a) Nitrogen absorption-desorption isotherms and (b) the pore size distribution curves of MCO, MCS and MCS@NCS on Ni foam.

Figure 3.5a compares the cyclic voltammetry (CV) curves of the MCO, MCS and MCS@NCS electrodes at a scan rate of 10 mV/s. It is found that the CV curve of all the electrodes has redox peaks which are ascribed to the reversible redox reactions of the active materials. It can be clearly seen that the MCS@NCS sample has the largest enclosed CV curve area owing to more specific surface area and richer redox reactions. The typical faradaic CV curves of MCS@NCS electrode at different scan rates ranging from 5 mV/s to 50 mV/s at a potential window of -0.1-0.65 V are depicted in Figure 3.5b. In each CV curve, the redox peaks are obvious owing to various redox reactions occurred under the scanning potential, implying that the capacitance of the hybrid electrode primarily comes from faradaic pseudocapacitance related to M-S, where M represents Mn, Co and Ni. The electrochemical redox reactions occurred during the charge-discharge process are listed below [3, 6-8]:

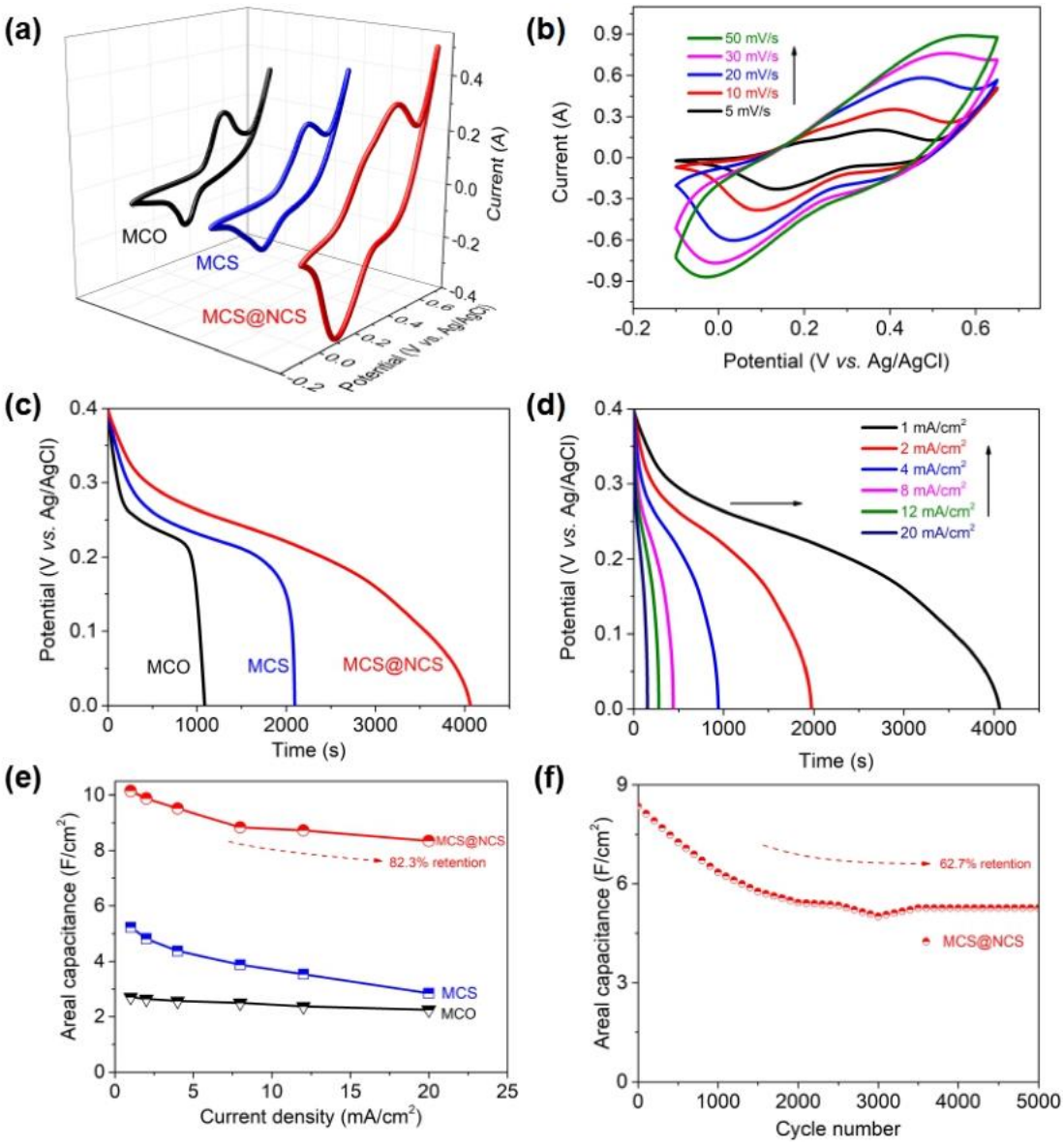

Figure 3.5. (a) CV curves of MCO, MCS and MCS@NCS at the scan rate of 10 mV/s. (b) CV curves of the MCS@NCS electrode measured at different scan rates. (c) Galvanostatic discharge curves of MCO, MCS and MCS@NCS at the current density of 1 mA/cm^2. (d) Galvanostatic discharge curves of the MCS@NCS electrode at the different current densities. (e) Areal capacitance of MCO, MCS and MCS@NCS electrodes as a function of current density. (f) Cycling performance of the MCS@NCS electrode at a scan rate of 50 mV/s for 5000 cycles.

$$MnCo_2S_4 + OH^- + H_2O \leftrightarrow MnSOH + 2CoSOH + 2e^-$$

$$NiS + OH^- \leftrightarrow NiSOH + e^-$$

$$CoS + OH^- \leftrightarrow CoSOH + e^-$$

$$CoSOH + OH^- \leftrightarrow CoSO + H_2O + e^-$$

The molar ratio of $Ni(NO_3)_2 \cdot 6H_2O$ and $Co(NO_3)_2 \cdot 6H_2O$ in the electrochemical deposition of nickel cobalt sulfide (shell material) can significantly influence the electrochemical performance. As shown in Figure 3.6, the CV area of the Ni-Co-S on nickel foam is the largest when the molar ratio for $Ni(NO_3)_2 \cdot 6H_2O$ and $Co(NO_3)_2 \cdot 6H_2O$ is 1:1. It is found that different molar ratios of Ni^{2+} and CO^{2+} result in different redox reaction potentials. The Ni-S (Co:Ni=0:1) material shows a redox couple at 0.41 and 0.2 V, while the Co-S (Co:Ni=1:0) exhibits the redox couples at 0.06, 0.18, 0.25 and 0.4 V. In addition, the CV curve of electrochemically deposited Ni-Co-S is not a simple addition of individual CV curve of Ni-S and Co-S.

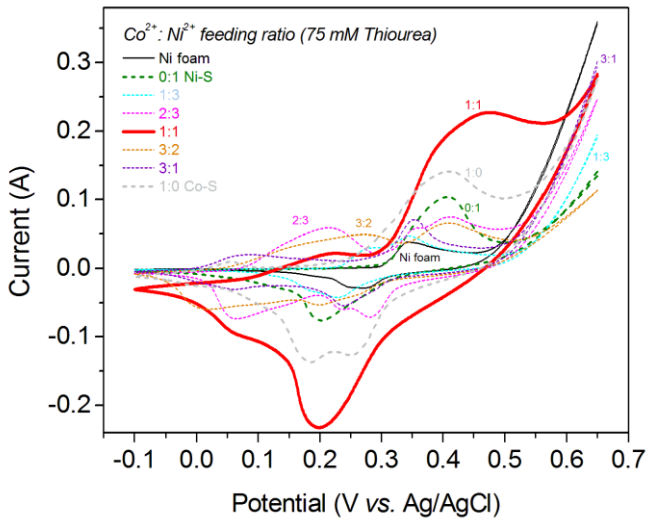

Figure 3.6. CV response of Ni-Co-S on Ni foam prepared at different molar ratios of Ni^{2+} and Co^{2+} during the electrochemical deposition.

The galvanostatic discharge curves of MCO, MCS and MCS@NCS at current density of 1 mA/cm^2 are compared in Figure 3.5c. Among all the samples, the MCS@NCS core-shell hybrid electrode shows the longest discharge time. The plateau in the discharge curves indicates the pseudocapacitive properties of the electrode materials, which is consistent with the multiple redox peaks depicted in the CV curves. Based on Figure 3.5c, the capacitance of MCO, MCS, and MCS@NCS is 2.71, 5.23, and 10.14 F/cm^2, respectively. The areal capacitance of the MCS@NCS electrode is the largest among the studied electrodes and about 4 times larger than that of the MCO electrode. Figure 3.5d presents the galvanostatic discharge curves of the MCS@NCS electrode at different current densities (1, 2, 4, 8, 12 and 20 mA/cm^2) and the corresponding capacitance is 10.14, 9.88, 9.52, 8.84, 8.73 and 8.35 F/cm^2, respectively. The proposed MCS@NCS electrode has larger capacitance compared to most reported composite electrodes based on manganese, cobalt, nickel and sulfur. Table 3.1 shows a detailed comparison. The areal capacitance of MCO, MCS and MCS@NCS hybrid electrode as a function of current density is compared in Figure 3.5e. The MCS@NCS electrode can retain 82.3 % of the initial capacitance even at a current density of 20 mA/cm^2, indicating a good rate capability. The improved performance of the MCS@NCS electrode could be attributed to three main reasons: (1) the core-shell nanocomposite having a mesoporous structure with high specific surface area can reduce the ionic diffusion pathway and increase the active-site accessibility; (2) Ni-Co sulfide (the shell material) can enhance the redox activities

and thus the pseudocapacitance by combining the advantages of Ni-S and Co-S; and (3) manganese cobalt sulfide (the core material) has high electrical conductivity, hence facilitating electron transport and current collection. Another important parameter to assess the electrochemical performance of electrode materials for energy storage devices is the long-term cycling stability. The durability test of MCS@NCS was conducted by measuring the CV curve at a scan rate of 50 mV/s for 5000 successive cycles and the results are presented in Figure 3.5f. There is a large drop in areal capacitance from 8.35 F/cm^2 to 5.42 F/cm^2 in the first 2000 cycles and the capacitance is remained stable at 5.26 F/cm^2 after 5000 cycles, resulting in an overall

Electrode materials	C_a (F/cm^2)	References
$MnCo_2S_4$@Ni-Co-S	10.14 (1 mA/cm^2)	This work
$NiCo_2S_4$@$Co(OH)_2$ nanotube	9.6 (2 mA/cm^2)	[9]
$NiCo_2S_4$@CoS_x	4.74 (5 mA/cm^2)	[10]
$NiCo_2S_4$@Ni-Mn LDH arrays	1.74 (1 mA/cm^2)	[11]
$NiCo_2S_4$@MnO_2	2.6 (3 mA/cm^2)	[12]
$NiCo_2S_4$@$Ni_{(1-x)}Co_x(OH)_2$ nanoarrays	3.54 (1 mA/cm^2)	[13]
$NiCo_2S_4$ nanotube@$NiCo_2S_4$ nanosheet	4.38 (5 mA/cm^2)	[14]

Table 3.1. Comparison of capacitance of electrodes based on manganese, cobalt, nickel and sulfur.

retention rate of ~ 62.7 %. The initial drop in capacitance could be due to the collapse of some core/shell structures during the charge-discharge process (Figure 3.7). Based on the previous reports [6, 15-17], it is believed that the durability of the electrodes shows the following trend: MCS@NCS > MCS > MCO.

Figure 3.8 shows the Nyquist plots of MCO, MCS and MCS@NCS in the frequency range of 0.01 Hz to 10 kHz measured at open circuit potential with AC amplitude of 10 mV. The first x-intercept of the Nyquist plot stands for the internal resistance (R_s) or equivalent series resistance. From the inset of Figure 3.8, R_s of MCO, MCS and MCS@NCS electrodes is as small as 0.48, 0.31 and 0.76 Ω respectively. The slope of the curve in the low frequency region can be used to deduce the Warburg impedance (W), which is associated with diffusion of electrolyte

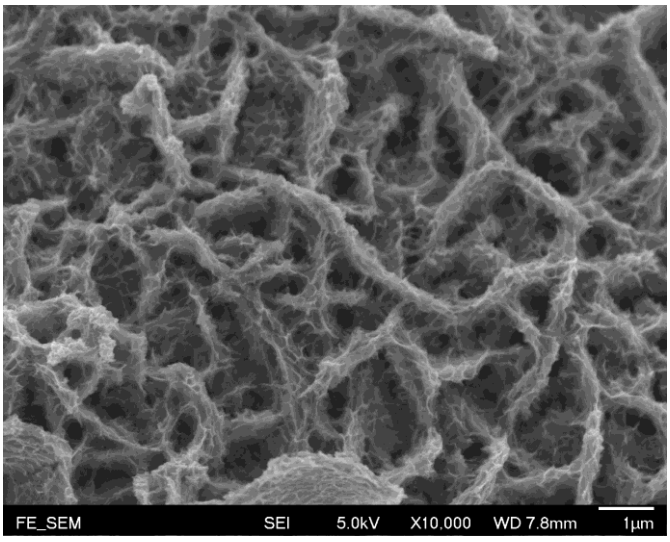

Figure 3.7. SEM image of MCS@NCS electrode after 2000 cycles of charging-discharging.

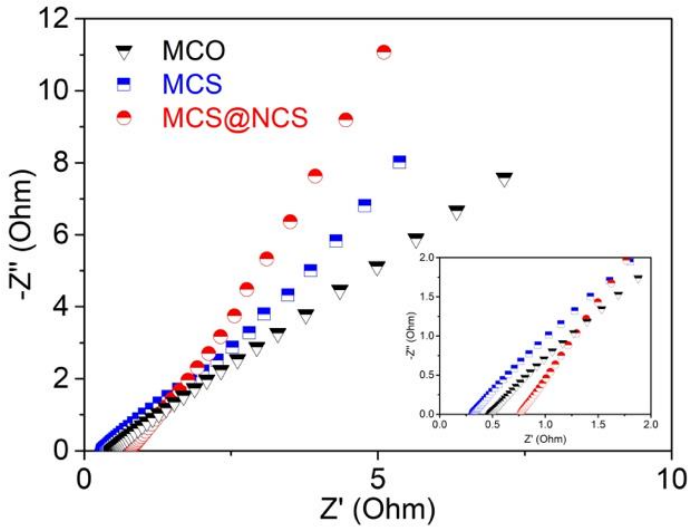

Figure 3.8. Nyquist plots of MCO, MCS and MCS@NCS electrodes. Inset is the high resolution Nyquist plots.

ions in the electrode materials during the charge and discharge processes. The MCS@NCS shows the steepest slope in low frequency area among the samples, revealing that it stores charges most efficiently [18].

An asymmetric supercapacitor (ACS) was fabricated using Ni foam@MCS@NCS as the positive electrode and Ni foam@activated carbon (AC) as the negative electrode in order to further study the electrochemical performance of the MCS@NCS hybrid electrode for supercapacitor applications. The CV curves and GCD curves of the negative AC electrode are shown in Figure 3.9a and b respectively. At all the scan rates from 5 to 50 mV/s, the CV profiles retain a similar shape and the GCD curves are symmetrical and linear, suggesting a good Coulombic efficiency of the electrode. According to Figure 3.9c, it is noticed that the positive

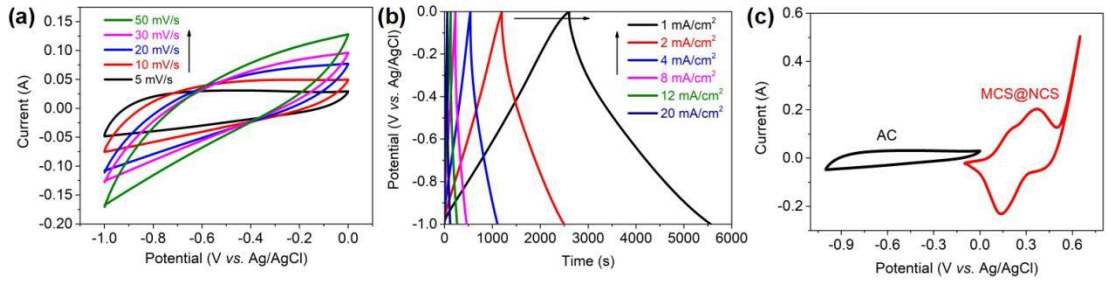

Figure 3.9. (a) CV curves of AC electrode at different scan rates. (b) Galvanostatic charge-discharge curves of AC electrode at different current densities. (c) CV curves of positive MCS@NCS and negative AC electrode at a scan rate of 5 mV/s.

electrode has a stable operating potential from -0.1 V to 0.65 V while the negative electrode has a stable potential window from -1 V to 0 V. Therefore, it is believed that the operating voltage of the ASC could be extended to 1.65 V. Based on the mass of MCS@NCS (3.8 mg/cm^2) and AC (9.5 mg/cm^2), the specific capacitance of MCS@NCS and AC determined from the discharge curves in Figure 3.5d and 3.9b at 1 mA/cm^2 is 2668.4 F/g and 308 F/g respectively. According to equation 3.1-3.3, the mass ratio of MCS@NCS to AC is calculated to be 6.5:1 in order to keep the charges balance at the positive and negative electrodes.

A schematic diagram of the ASC fabricated by using MCS@NCS on nickel foam as the positive electrode, AC on nickel foam as the negative electrode and cellulose paper as the separator is shown in Figure 3.10a. Figure 3.10b shows the CV curves of the ASC at various scan rates. The working voltage of the device could be increased to 1.65 V with stable electrochemical properties. With increasing scan rates, the CV curves maintain similar shape, demonstrating a good capacitive

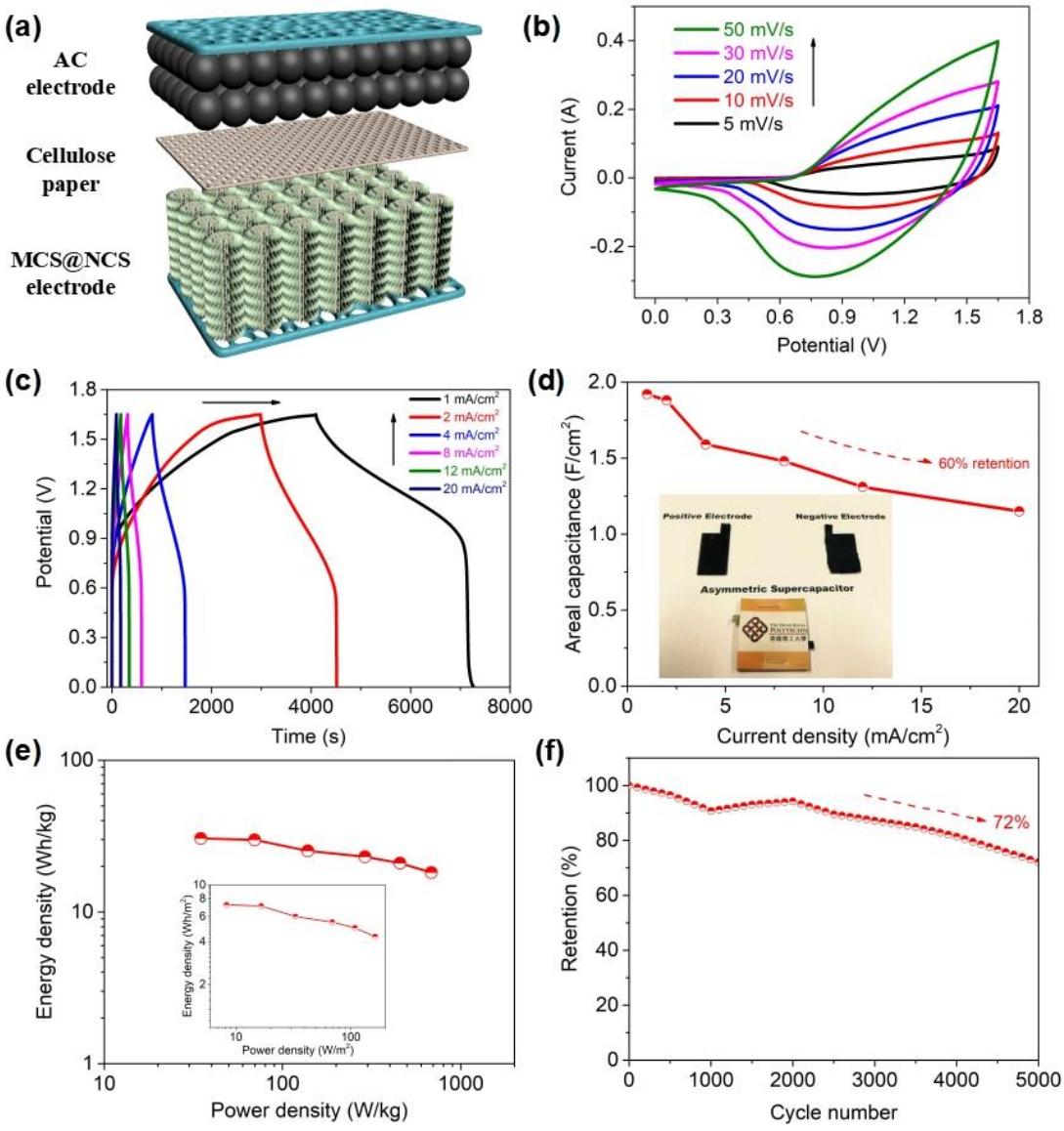

Figure 3.10. (a) Schematic diagram of an ASC. (b) CV curves of the ASC at different scan rates. (c) GCD curves of the ASC at different current densities. (d) Areal capacitance of the ASC as a function of current density. Inset is the digital image of the electrodes and ASC. (e) Energy density versus power density of the studied ASC based on the mass of the active materials in the device. Inset is the plot of energy density and power density based on the area of device. (f) Cycling performance of the ASC at 50 mV/s over 5000 cycles.

behavior. Figure 3.10c depicts the GCD curves of the ASC at different current densities (1, 2, 4, 8, 12 and 20 mA/cm^2). The nonlinear charge and discharge curves further verify the pseudocapacitive properties, which is consistent with the reduction-oxidation peaks in the CV curves shown in Figure 3.10b. Figure 3.10d presents the areal capacitance of the MCS@NCS//AC ASC at various current densities deduced from the discharge curves in Figure 3.10c. The ASC device shows a remarkable capability of 1.92 F/cm^2 at a current density of 1 mA/cm^2 and retains 60 % of the areal capacitance (1.15 F/cm^2) at a current density of 20 mA/cm^2, demonstrating good rate capability of the asymmetric supercapacitor device. According to Figure 3.10c and equation 3.4-3.7, the energy density and power density of the asymmetric supercapacitor device are calculated and depicted in Figure 3.10e. The ASC device can deliver a maximum energy density and power density of 7.26 Wh/m^2 (30.5 Wh/kg) and 162.7 W/m^2 (683.7 W/kg) respectively. The energy density of the studied ASC device is comparable or higher than many reported devices based on nickel/manganese/cobalt oxides/hydroxides/sulfides such as $NiCo_2S_4$@$NiCo_2S_4$//reduced graphene oxide (RGO) (24.9 Wh/kg) [13], Ni(OH)@3D Ni//AC (21.8 Wh/kg) [19], $NiCo_2O_4$@$NiMoO_4$//AC (21.7 Wh/kg) [20], $NiCo_2O_4$//RGO (23.9 Wh/kg) [21], Co_3O_4//graphene hydrogel (31 Wh/kg) [22], $NiCo_2O_4$-RGO//AC (23.3 Wh/kg) [23], $NiCo_2O_4$@$Co_{0.33}Ni_{0.67}(OH)_2$//CMK-3 (31.2 Wh/kg) [24], $NiCo_2O_4$ hollow spheres//AC (43.8 Wh/kg) [25], $MnCo_2S_4$//RGO (31.3 Wh/kg) [26] and $Co(OH)_2Co_3O_4$//AC (22.4 Wh/kg) [27]. The cycling stability of

MCS@NCS//AC is also tested under the scan rate of 50 mV/s for 5000 cycles. Based on Figure 3.10f, after a slight reduction in areal capacitance, the areal capacitance increases again owing to the activation process of the electrode materials. The device can remain 72 % of the initial capacitance after 5000 cycles, indicating good stability of the studied asymmetric supercapacitor.

3.4 Summary

An electrode based on $MnCo_2S_4$@Ni-Co-S core-shell nanostructure was fabricated via a simple and facile method including a hydrothermal treatment and an electrochemical deposition. $MnCo_2S_4$ (the core material) not only shows different redox reactions during charge and discharge process but also serves as the ideal skeleton to load Ni-Co-S (the shell material) for enhancing the electrochemical performance. The as-prepared MCS@NCS core-shell hybrid electrode exhibits ultrahigh areal capacitance (10.14 F/cm^2 at a current density of 1 mA/cm^2) and the ASC fabricated using Ni foam@MCS@NCS as positive electrode and Ni foam@AC as negative electrode also demonstrates excellent energy density (7.26 Wh/m^2), and good cycling stability (72 % capacitance retention after 5000 cycles) owing to the synergistic effect from $MnCoS_4$ and Ni-Co-S. Hence, $MnCo_2S_4$@Ni-Co-S core-shell structure has great potential application for high-performance supercapacitors.

3.5 References

[1] J. Zhao, J. Chen, S. Xu, M. Shao, D. Yan, M. Wei, D. G. Evans, X. Duan, *J*. *Mater*. *Chem*. *A*, 2013, **1**, 8836.

[2] H. Wan, J. Jiang, J. Yu, K. Xu, L. Miao, L. Zhang, H. Cheng, Y. Ruan, *CrystEngComm*, 2013, **15**, 7649.

[3] R. Li, S. Wang, Z. Huang, F. Lu, T. He, *J*. *Power Sources*, 2016, **312**, 156.

[4] C. C. Hu, J. C. Chen, K. H. Chang, *J*. *Power Sources*, 2013**, 221**, 128.

[5] L. Peng, L. Lv, H. Wan, Y. Ruan, X. Ji, J. Liu, L. Miao, C. Wang, J. Jiang, *Mater*. *Today*, 2017, **4**, 122.

[6] W. Fu, C. Zhao, W. Han, Y. Liu, H. Zhao, Y. Ma, E. Xie, *J*. *Mater*. *Chem*. *A*, 2015, **3**, 10492.

[7] L. Mei, T. Yang, C. Xu, M. Zhang, L. Chen, Q. Li, T. Wang, *Nano Energy*, 2014, **3**, 36.

[8] F. Grote, Z. Y. Yu, J. L. Wang, S. H. Yu, Y. Lei, *Small*, 2015, **11**, 4666.

[9] R. Li, S. Wang, Z. Huang, F. Lu, T. He, *J*. *of Power Sources*, 2016, **312**, 156.

[10] W. Fu, C. Zhao, W. Han, Y. Liu, H. Zhao, Y. Ma, E. Xie, *J*. *Mater*. *Chem*. *A*, 2015, **3**, 10492.

[11] H. Wan, J. Liu, Y. Ruan, L. Lv, L. Peng, X. Ji, L. Miao, J. Jiang, *ACS Appl*. *Mater*. *Interfaces*, 2015, **7**, 15840.

[12] K. Xu, Q. Ren, Q. Liu, W. Li, R. Zou, J. Hu, *RSC Adv*., 2015, **5**, 44642.

[13] W. Zhou, K. Yu, D. Wang, J. Chu, J. Li, L. Zhao, C. Ding, Y. Du, X. Jia, G. Wen, *Nanotechnology*, 2016, **27**, 235402.

[14] H. Chen, S. Chen, H. Shao, C. Li, M. Fan, D. Chen, G. Tian, K. Shu, *Chemistry–An Asian Journal*, 2016, **11**, 248.

[15] X. Wang, B. Shi, F. Huang, Y. Fang, F. Rong, R. Que, *J. of Alloys and Compound*, 2018, **767**, 232.

[16] Z. Sadighi, J. Liu, F. Ciucci, J.K. Kim, *Nanoscale*, 2018, **10**, 15588.

[17] X. Zheng, Y. Ye, Q. Yang, B. Geng, X. Zhang, *Dalton Trans*., 2016, **45**, 572.

[18] K. Sheng, Y. Sun, C. Li, W. Yuan, G. Shi, *Sci. Rep*., 2012, **2**, 247.

[19] Y. Su, K. Xiao, N. Li, Z. Q. Liu, S. Z. Qiao, *J. Mater. Chem. A*, 2014, **2**, 13845.

[20] D. Cheng, Y. Yang, J. Xie, C. Fang, G. Zhang, J. Xiong, *J. Mater. Chem. A*, 2015, **3**, 14348.

[21] H. Chen, J. Jiang, L. Zhang, T. Qi, D. Xia, H. Wan, *J. of Power Sources*, 2014, **248**, 28.

[22] Y. Liang, Y. Yang, Z. Hu, Y. Zhang, Z. Li, N. An, H. Wu, *Int. J. Electrochem. Sci*, 2016, **11**, 4092.

[23] X. Wang, W. S. Liu, X. Lu, P. S. Lee, *J. Mater. Chem*., 2012, **22**, 23114.

[24] K. Xu, R. Zou, W. Li, Q. Liu, X. Liu, L. An, J. Hu, *J. Mater. Chem. A*, 2014, **2**, 10090.

[25] X. Li, L. Jiang, C. Zhou, J. Liu, H. Zeng, *NPG Asia Mater*., 2015, **7**, e165.

[26] S. Liu, S. C. Jun, *J. of Power Sources*, 2017, **342**, 629.

[27] M. Jing, Y. Yang, Y. Zhu, H. Hou, Z. Wu, X. Ji, *Electrochem. Acta*, 2014, **141**, 234.

Chapter 4

Flexible Solid-State Supercapacitors Using Paper-Based Electrodes for Energy Storage Applications

4.1 Introduction

Flexible supercapacitors have received significant attention from scientists in recent years due to their potential application in miniaturized, flexible, portable, and wearable electronics [1, 2]. A flexible supercapacitor usually consists of 4 main parts: (1) positive electrode, (2) negative electrode, (3) separator and (4) electrolyte. Metal foils and plastics are often employed as substrates to fabricate flexible supercapacitors. Nevertheless, they may have some disadvantages for example ease of oxidation and corrosion, less flexibility and weak attraction between electrode materials and substrates [3-5]. Owing to its lightweight, flexibility, wide availability, environmentally safe, recyclability and low cost, paper mainly composed of cellulose fibers is a promising substrate for flexible supercapacitors [6]. Conductive materials for example carbon nanotubes, graphite and conducting polymer could be easily deposited onto a piece of paper by different methods such as spin coating, vacuum filtration, polymerization and printing to form a highly conductive paper [7]. In this Chapter, flexible paper-based electrodes are prepared by coating CNTs and nickel cobalt sulfide on a filter paper using a simple and low-cost method involving soaking

and electrodeposition. A flexible solid-state symmetric supercapacitor based on these paper-based electrodes is fabricated and studied.

4.2 Experimental

4.2.1 Fabrication of CNTs-Coated Paper (Paper@CNTs)

Filter papers with dimension of 15 mm×20 mm×1 mm were ultrasonically cleaned with 1 M hydrochloric acid and dried at 60 ^{o}C. A CNT suspension was prepared by mixing polyvinyl alcohol glue (3 mL), Na_2SO_4 (10 mmol), carbon nanotubes (5 g), carbon black (2 g) and deionized (DI) water (20 mL) and heated at 60 ^{o}C with vigorous stirring for 3 hours. Carbon black is a conducting agent which can facilitate electrons transfer. The filter papers were soaked into the CNT suspension for 5 minutes and then taken out to dry at 60 ^{o}C. This soak-and-dry process was repeated three times.

4.2.2 Preparation of Paper@CNTs@NCS

The CNTs-coated paper acts as a conductive platform for the growth of Ni-Co sulfide (NCS) via a simple electrochemical deposition method. Firstly, an aqueous electrolyte was prepared by dissolving $Ni(NO_3)_2H_2O$ (10 mmol), $Co(NO_3)_2H_2O$ (10 mmol) and thiourea (10 mmol) in 50 mL of DI water. Then, a standard three-electrode configuration was used to conduct the deposition process with an Ag/AgCl as reference electrode, the CNTs-coated paper as the working electrode and a

platinum foil as counter electrode. The deposition was conducted by applying a potential between -1.2 V and 0.2 V with the scan rate of 10 mV/s for 30 cycles. The fabrication process of the CNTs@NCS paper electrode is schematically illustrated in Figure 4.1.

4.2.3 Assembly of Solid-State Symmetric Supercapacitors

The polyvinyl alcohol (PVA)/KOH gel electrolyte was first prepared by adding KOH (5 g) and PVA glue (10 mL) into DI water (50 mL) under stirring at 80 ^{o}C for 4 hours. Two pieces of CNTs@NCS-coated paper were then soaked in the gel electrolyte for 3 minutes and sandwiched with a thin film of insulating plate as a separator to form a symmetric supercapacitor.

4.3 Results and Discussion

The electrochemical studies for the Paper@CNTs and Paper@CNTs@NCS electrodes were conducted in a typical three-electrode cell with 3 M KOH as the aqueous electrolyte. The cyclic voltammetry (CV) curves of the electrodes at the scan

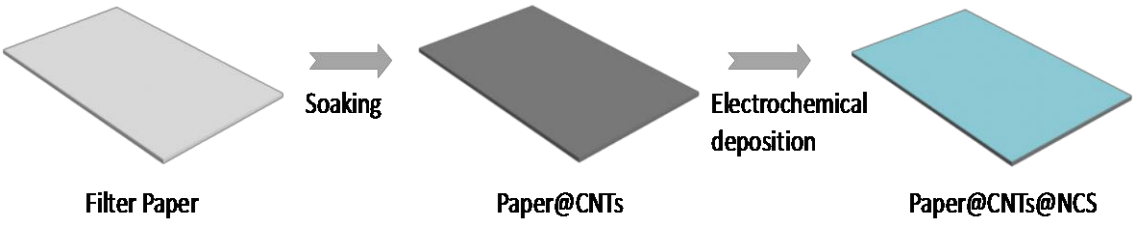

Figure 4.1. Schematic diagram of the fabrication procedure for the Paper@CNTs@NCS electrode.

rate of 50 mV/s are shown in Figure 4.2a. Only the Paper@CNTs@NCS electrode has reduction-oxidation peaks in the CV curves. These redox peaks should be attributed to the fast and reversible faradaic redox reactions of Ni-Co sulfide. The Paper@CNTs@NCS electrode has a larger CV area than the Paper@CNTs electrode, indicating an improved charge storage capacity. The CV curves of Paper@CNTs@NCS at different scan rates (5, 10, 20, 30 and 50 mV/s) are shown in Figure 4.2b. It is found that at all the scan rates from 5 to 50 mV/s the CV profiles maintain a similar shape, implying a good capacitive behavior of the electrode [8]. Figure 4.2c displays the galvanostatic discharge curves of the Paper@CNTs and Paper@CNTs@NCS electrodes at the current density of 0.1 mA/cm^2. The plateau in the discharge curve of the Paper@CNTs@NCS electrode demonstrates the pseudocapacitive properties of the electrode materials [9]. Figure 4.2d shows the discharge curves of the Paper@CNTs@NCS electrode at the current densities from 0.1 mA/cm^2 to 1 mA/cm^2. The areal capacitance of an electrode could be extracted from the discharge curve. The areal capacitance of the electrodes at different current densities is depicted in Figure 4.2e. The Paper@CNTs@NCS exhibits a capacitance of 38.3 mF/cm^2 which is 2.5 times larger than its counterpart without NCS at the current density of 0.1 mA/cm^2. When the current density is increased to 1 mA/cm^2, the Paper@CNTs@NCS electrode can still retain 72 % of the initial capacitance, indicating a good rate capability. The improved performance of the Paper@CNTs@NCS electrode should be ascribed to the synergistic effect from the

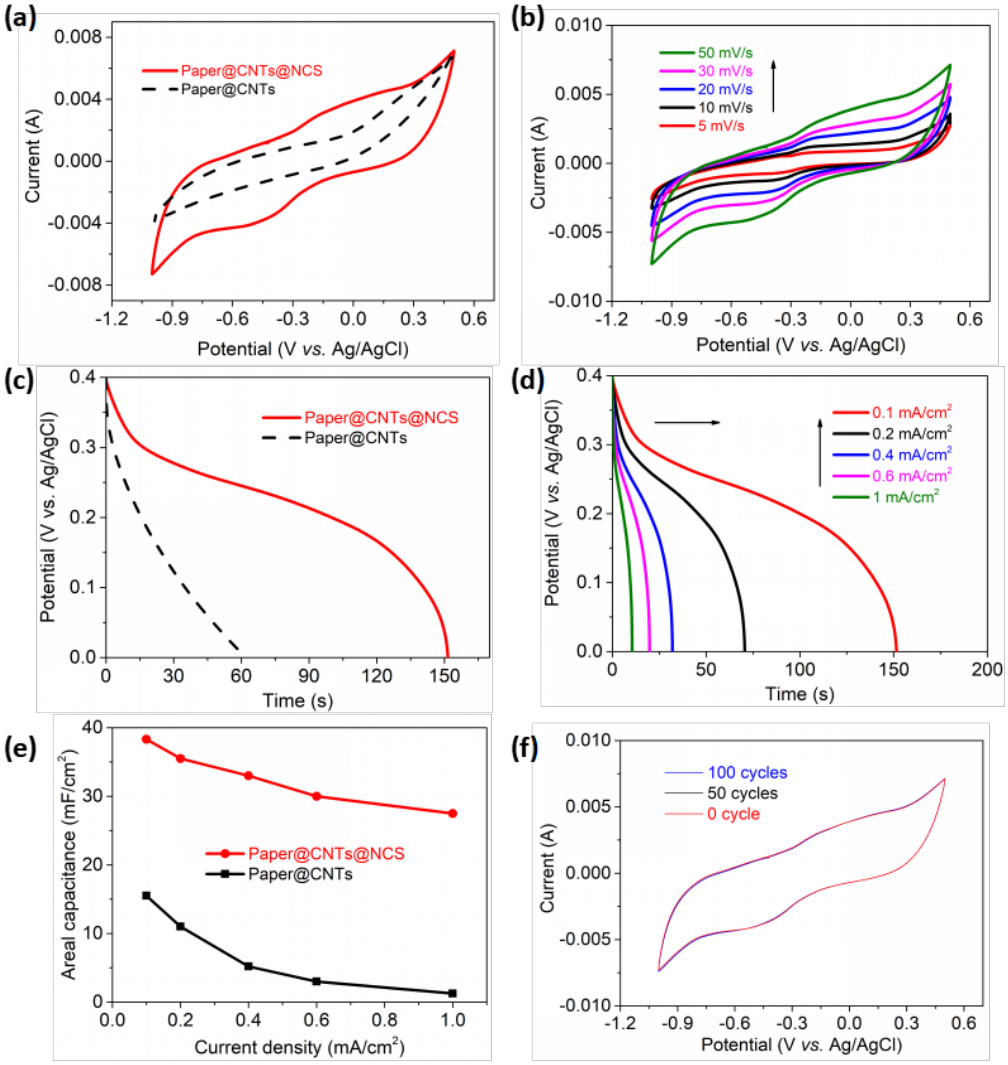

Figure 4.2. (a) CV curves of Paper@CNTs and Paper@CNTs@NCS electrodes at a scan rate of 50 mV/s. (b) CV curves of the Paper@CNTs@NCS electrode with scan rates varied from 5 mV/s to 50 mV/s. (c) Galvanostatic discharge curve of the Paper@CNTs and Paper@CNTs@NCS electrodes collected at the current density of 0.1 mA/cm^2. (d) Galvanostatic discharge curve of the Paper@CNTs@NCS electrodes at different current densities. (e) Areal capacitance of electrodes as a function of current density. (f) CV curves of Paper@CNTs@NCS electrode after various bending cycles at 50 mV/s.

double-layer capacitance of CNTs and the pseudo-capacitance of Ni-Co sulfide. The flexibility test of the Paper@CNTs@NCS electrode was conducted by bending the electrode from 0^o to 180^o for various cycles. Figure 4.2f shows the CV curves of the electrode measured at a scan rate of 50 mV/s after 0, 50 and 100 bending cycles. It is noteworthy that the CV curve remains almost the same after bending for 100 cycles. This indicates that the Paper@CNTs@NCS electrode is bendable and mechanically stable.

To further demonstrate the capacitive performance of CNTs@NCS on paper, a flexible solid-state symmetric supercapacitor using Paper@CNTs@NCS as both positive and negative electrodes was fabricated. Figure 4.3a shows the CV curves of the solid-state symmetric SC based on Paper@CNTs@NCS at various scan rates (5, 10, 20, 30 and 50 mV/s). The operating potential is between -0.1 and 0.65 V. With increasing scan rates, the cyclic voltammetry curves remain similar in shape. This confirms again a good capacitive behavior. The galvanostatic charge/discharge (GCD) curves of the Paper@CNTs@NCS-based symmetric device at different current densities (0.1, 0.2, 0.3 and 0.4 mA/cm^2) are presented in Figure 4.3b. Figure 4.3c shows the areal capacitance of the SC device at various current densities calculated from the discharge curves in Figure 4.3b. The capacitance of the supercapacitor based on Paper@CNTs@NCS is 8.4 mF/cm^2 at the current density of 0.1 mA/cm^2. Figure 3d depicts the areal energy density versus the power density of the studied SC device. It is found that the maximum energy density and power density of the SC

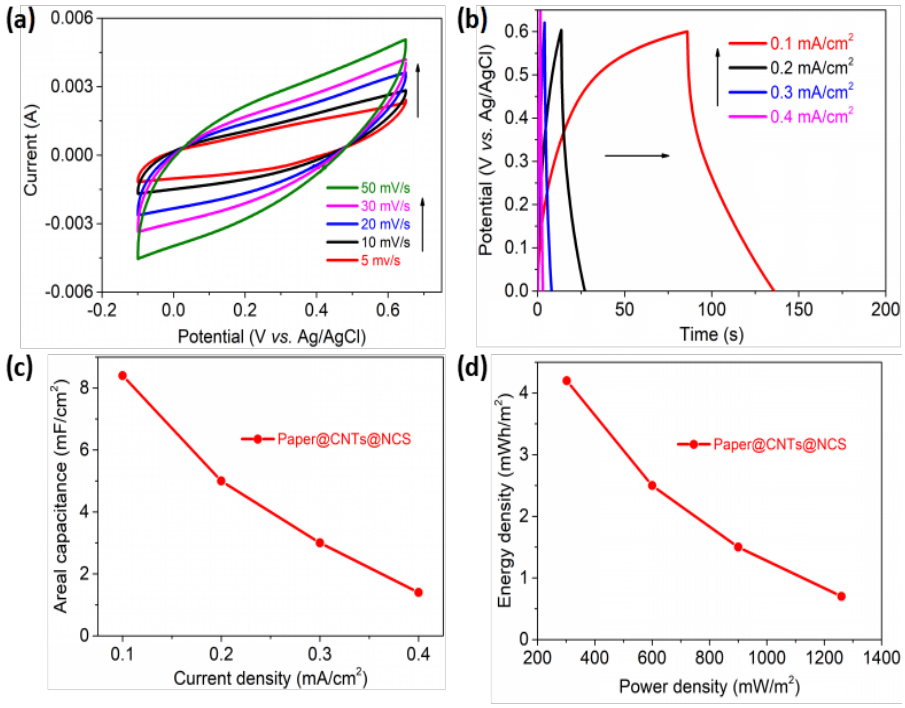

Figure 4.3. (a) CV curves of CNTs@NCS//CNTs@NCS symmetric SC at different scan rates. (b) GCD curves of the symmetric SC made by CNTs@NCS paper electrodes at different current densities. (c) Areal capacitance of the SC as a function of current density. (d) Ragone plot of the studied supercapacitor.

based on Paper@CNTs@NCS is 4.2 mWh/m^2 and 1.26 W/m^2 respectively. These results reveal the possibility of the studied paper-based supercapacitor device for flexible energy storage.

4.4 Summary

In summary, CNTs and Ni-Co-S are deposited on the paper substrate after a simple soaking and electrochemical deposition. The as-prepared NCS-CNTs paper

electrode shows excellent areal capacitance (38.3 mF/cm^2 at 0.1 mA/cm^2), mechanical stability and flexibility. By combining the benefits of carbon nanotubes and nickel cobalt sulfide, the flexible solid-state symmetric SC device using Paper@CNTs@NCS electrodes demonstrates great potential applications as an energy storage device for flexible electronic systems.

4.5 References

[1] L. Lin, Z. Wu, S. Yuan and X. B. Zhang, *Energy Environ*. *Sci*., 2014, **7**, 2101–2122.

[2] X. Wang, X. Lu, B. Liu, D. Chen, Y. Tong and G. Shen, *Adv*. *Mater*., 2014, **26**, 4763–4782.

[3] L. Hu, J. W Choi, Y. Wang, S. Jeong, F. La Mantia, L.-F. Cui, Y. Cui, *Proc*. *Natl*. *Acad*. *Sci*. *U*.*S*.*A*., 2009, **106**, 21490.

[4] G. Yu, L. Hu, M. Vosgueritchian, H. Wang, X. Xie, J.R. McDonough, X. Cui, Y. Cui, Z. Bao, *Nano Letters*, 2011, **11**, 2905–2911.

[5] A. Russo, B. Ahn, J. Adams, E. Duoss, J. T. Bernhard, J. A. Lewis, *J*. *Adv*. *Mater*. 2011, **23**, 3426−3430

[6] V. L.Pushparaj, M. M. Shaijumon, A. Kumar, S. Murugesan, L. Ci, L. R. Vajtai, R. J. Linhardt, O. Nalamasu, P.M. Ajayan, *Proc*. *Natl*. *Acad*. *Sci*. *U*.*S*.*A*., 2007, **104**, 13574–13577.

[7] L. Nyholm, G. Nystrom, A. Mihranyan, M. Stromme, *Adv*. *Mater*., 2011, **23**, 3751–3769.

[8] X. He, C.P. Yang, G.L. Zhang, D.W. Shi, Q.A. Huang, H.B. Xiao, Y. Liu, R. Xiong, *Mater*. *Des*., 2016, **106**, 74–80.

[9] W. Fu, Y. Wang, W. Han, Z. Zhang, H. Zha, E. Xie, *J*. *Mater*. *Chem*. *A*, 2016, **4**, 173-182.

Chapter 5
Solid-State Flexible Supercapacitor Based on Inkjet Printed Interdigital Electrodes

5.1 Introduction

Since the rapid developments in lightweight, portable and bendable electronic devices, there is an increasing demand for flexible, high-performance, wearable and solid-state supercapacitors [1-5]. In order to achieve large-scale and fast production for industrial applications, many manufacturing techniques such as screen printing, inkjet printing and knitting have been investigated to fabricate supercapacitors [2, 6-8]. Inkjet printing provides a novel route to fabricate low-cost, large-area and high-throughput solid-state supercapacitors. Compared to the conventional sandwich structure, supercapacitor electrode with interdigitated structure has several benefits including small internal resistance, short migration distance of ions and large surface area [9-11], resulting in high electrochemical performance. In this Chapter, a pseudocapacitive ink consisted of Mn^{2+} and Co^{2+} is directly printed on a thin Al foil by an inkjet printer in the interdigitated structure, followed by heat treatment to form the electrodes of the supercapacitors. Supercapacitors with different dimensions of interdigitated electrodes are fabricated and characterized.

5.2 Experimental

5.2.1 Preparation of Interdigitated Electrodes

A pink pseudocapacitive water-based ink was first prepared by mixing $MnCl_2 \cdot 4H_2O$ (25 mmol), $CoCl_2 \cdot 6H_2O$ (50 mmol) and deionized water (50 ml) with vigorous stirring. A commercial PixDro LP50 ink-jet printer with maximum accuracy of 5 μm was used to print the pink pseudocapacitive ink on a thin Al foil (~ 0.02 mm thick) in different interdigital patterns. The as-prepared electrodes were heated in an oven at 300 ^{o}C for two hours. A precise cutter was then used to remove the blank Al foil and the electrodes were fixed on the filter paper by glue.

5.2.2. Preparation of KOH-PVA Solid-State Electrolyte

First 3 mL of polyvinyl alcohol (PVA) glue was added into 20 mL of deionized water and the mixture was heated at 60 ^{o}C with intensive stirring for three hours. Then, 10 mL of 2 M KOH solution was added drop by drop into the mixture at room temperature under stirring until the mixture became transparent.

5.2.3. Assembly of Symmetric Supercapacitor Devices

The KOH-PVA solid-state electrolyte was coated uniformly on the as-prepared electrodes by a dropper and the electrodes with gel electrolyte were dried at 60 ^{o}C to form the in-plane supercapacitors.

5.3 Results and Discussion

Three interdigital patterns with different length and width of each electrode finger as well as the spacing between each electrode finger were designed. Supercapacitors based on these three interdigital patterns were fabricated (denoted as SC_1, SC_2 and SC_3) and the dimensions of their interdigital electrodes are shown in Figure 5.1.

A series of electrochemical tests for the fabricated interdigitated supercapacitors were conducted in a two-electrode configuration using Solarton Workstation. The cyclic voltammetry curves of the SC_1, SC_2 and SC_3 samples at different scan rates (10, 30 and 50 mV/s) are shown in Figure 5.2a, b and c. The

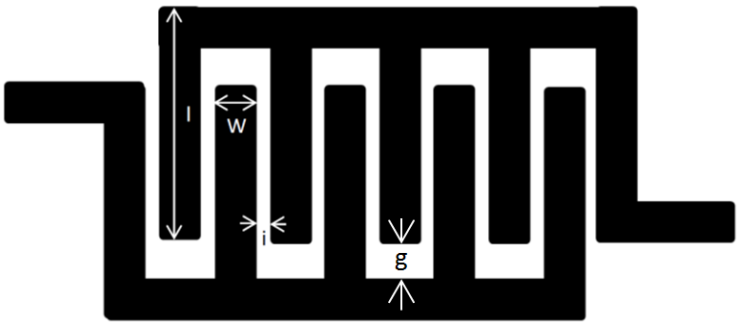

Sample	Length of electrode, l (mm)	Width of electrode, W (mm)	Number of electrodes	Space between electrodes, i (mm)	Horizontal gap, g (mm)	Total surface area (mm^2)
SC_1	14	3	10	1	1	666
SC_2	31	2	14	2.5	3	1084
SC_3	31	3	10	1	2	1116

Figure 5.1. Parameters of the interdigitated supercapacitors

operating window is between 0 and 0.5 V. The CV curves of all the interdigitated supercapacitors retain similar shape with increasing scan rates, showing a good capacitive behavior. Figure 5.2b, d and f show the galvanostatic charge/discharge (GCD) curves of the interdigitated supercapacitors at various charging/discharging current (0.005, 0.01, 0.02 and 0.03 mA). The GCD curves of SC_1, SC_2 and SC_3 at charging current of 0.005 mA are compared in Figure 5.3a. Figure 5.3b compares the CV curves of the supercapacitors with different electrode dimensions at the scan rate of 50 mV/s. Among the studied samples，SC_3 has the best electrochemical performance in term of capacitance because it has the largest area. The capacitance of the supercapacitor could be calculated from the discharge curve. The capacitance of SC_1, SC_2 and SC_3 at 0.005 mA charging current is 0.008, 0.009 and 0.045 mF respectively.

Figure 5.4 depicts the areal capacitance of SC_1, SC_2 and SC_3 supercapacitor devices at different scan rates. The areal capacitance C_{ac} was calculated from the CV curves through the following equation:

$$C_{ac}=A/(2s\Delta Va) \tag{5.1}$$

where A is the area of enclosed CV curve, s is the scan rate, ΔV the potential window and a is the area of the supercapacitor. At the scan rate of 10 mV/s, the areal capacitance of SC_1, SC_2 and SC_3 is about 0.013 mF/cm^2, 0.017 mF/cm^2 and 0.019 mF/cm^2. The SC_3 sample has the largest capacitance which should be due to its largest surface area for redox reactions.

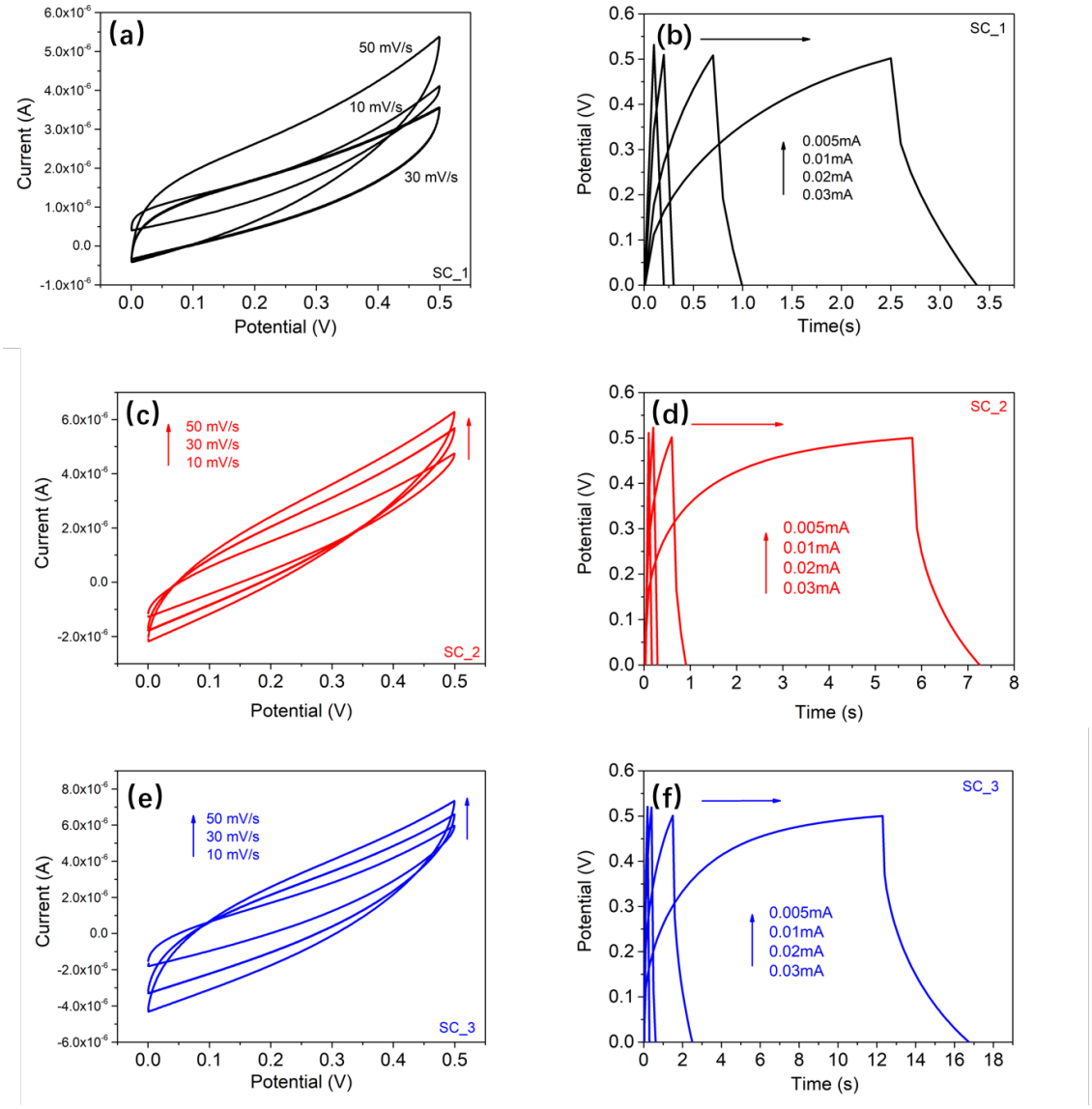

Figure 5.2. (a) (c) (e): CV curves of SC_1, SC_2 and SC_3 at different scan rates. (b) (d) (f): GCD curves of SC_1, SC_2 and SC_3 at different charging/discharging current.

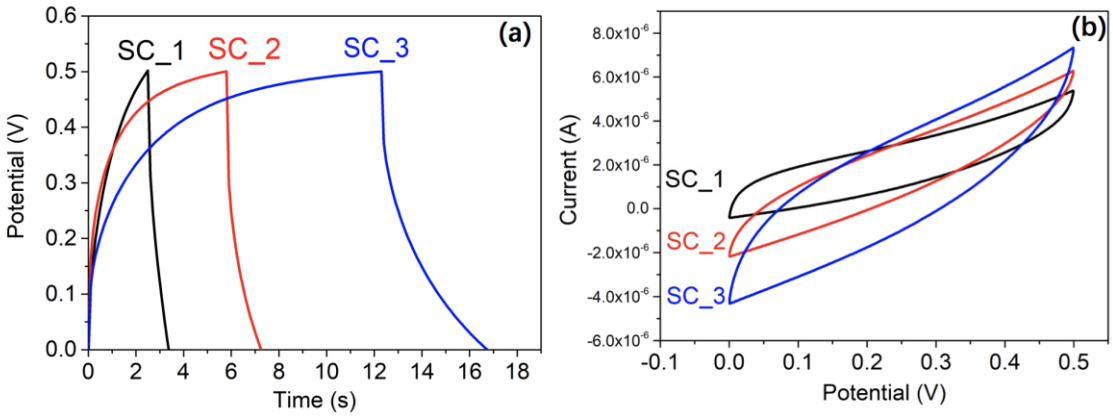

Figure 5.3. Comparison of electrochemical characteristics of SC_1, SC_2 and SC_3. (a) GCD curves at 0.005 mA. (b) CV curves at 50 mV/s.

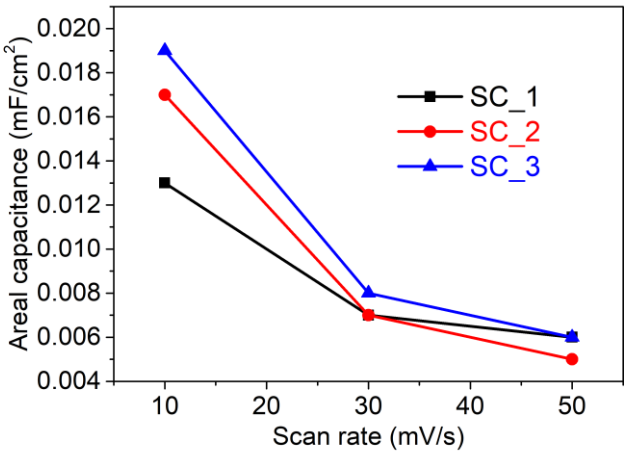

Figure 5.4. Areal capacitance of the SC_1, SC_2 and SC_3 as a function of scan rate.

5.4 Summary

A printable pseudocapacitive ink consisted of Mn^{2+} and Co^{2+} was prepared and deposited on the Al substrate by inkjet printing to form interdigitated electrodes. Symmetric supercapacitors with different space-length-width electrode fingers were fabricated and characterized. Experimental results show that the dimension of the interdigitated electrodes can affect the electrochemical performance. The supercapacitors with larger interdigitated-electrode area have higher charge storage capability. The interdigitated supercapacitor has great potential to be integrated with an energy harvester to form a self-powered nanosystem.

5.5 References

[1] Y. W. Zhu, S. Murali, M. D.Stoller, K. J.Ganesh, W. W. Cai, P. J. Ferreira, A. Pirkle, R. M. Wallace, K. A. Cychosz, M. Thommes, D. Su, E. A. Stach, R. S. Ruoff, *Science*, 2011, **332**, 1537.

[2] G. P. Wang, L. Zhang and J. J. Zhang, Chem. *Soc*. *Rev*., 2012, **41**, 797–828.

[3] Z. Fan, J. Yan, T. Wei, L. Zhi, G. Ning, T. Li, F. Wei, *Adv*. *Funct*. *Mater*., 2011, **21**, 2366–2375.

[4] C. Z. Meng, C. H. Liu, L. Z. Chen, C. H. Hu, S. S. Fan, *Nano Lett*., 2010, **10**, 4025.

[5] Z. Q. Niu, L. Zhang, L. Liu, B. W. Zhu, H. B. Dong and X. D. Chen, *Adv*. *Mater*., 2013, **25**, 4035–4042.

[6] Y. Xu, M.G. Schwab, A. J. Strudwick, I. Hennig, X. Feng, Z. Wu, K. Mullen, *Advanced Energy Materials*, 2013, **3**, 1035.

[7] J. Li, F. Ye, S. Vaziri, M. Muhammed, M.C. Lemme, M. Ostling, *Advanced Materials*, 2013, **25**, 3985.

[8] K. Dong, Y.C. Wang, J. Deng, Y. Dai, S.L. Zhang, H. Zou, B. Gu, B. Sun, Z. L. Wang, *ACS Nano*, 2017, **11**, 9490.

[9] C. Shen, X. Wang, W. Zhang, F. Kang, *J. of Power Sources*, 2011, **196**, 10465.

[10] M.F. El-Kady, R. B. Kaner, *Nature communications*, 2013, **4**, 1.

[11] W. Gao, N. Singh, L. Song, Z. Liu, A.L. M. Reddy, L. Ci, R. Vajtai, Q. Zhang, B. Wei, P.M. Ajayan, *Nature Nanotechnology*, 2011, **6**, 496.

Chapter 6
Conclusion

In this research, a series of tasks have been performed to improve the supercapacitors performance such as capacitance, energy density, working potential window, flexibility and scalability.

Firstly, solid-state symmetric supercapacitors based on three-dimensional $MnCo_2S_4$@$NiCo(OH)_2$ core-shell nanocomposite on the Ni foam substrate were studied. The core material $MnCo_2S_4$ combining the advantages of MnS_x and CoS_x was synthesized by a simple hydrothermal treatment followed by a sulfurization process. The $MnCo_2S_4$ nanorod arrays displayed good rate capability and could serve as effective scaffolds for loading a large amount of additional pseudo-capacitive material Ni-Co hydroxide to enhance the capacitance. The addition of the shell material $NiCo(OH)_2$ to $MnCo_2S_4$ could reinforce the mechanical stability of the whole electrode and improve the electrochemical properties of the supercapacitor.

On the basis of the above work, an electrode based on $MnCo_2S_4$@Ni-Co-S (MCS@NCS) core-shell nanostructure was fabricated for supercapacitor applications with a view to further promoting the electrochemical behavior. The as-prepared MCS@NCS core-shell hybrid electrode showed ultrahigh areal capacitance. SEM and TEM images showed that the Ni-Co-S nanosheet was uniformly grown on the surface of $MnCo_2S_4$ nanorods and had a highly porous surface which could facilitate

ions transportation and faradaic processes. In addition, the Brunauer-Emmett-Teller N_2 adsorption/desorption measurement revealed that the MCS@NCS hybrid structure had larger specific surface area compared to $MnCo_2S_4$ and $MnCo_2O_4$. The increased specific surface area of the hierarchical core-shell structure could provide more effective ion transport and electro-active sites for faradaic reactions, thus improving the electrochemical performance. Experimental results showed that the MCS@NCS electrode had smaller internal resistance and Warburg impedance compared to $MnCo_2S_4$ and $MnCo_2O_4$, indicating that it could store charges more efficiently. An asymmetric supercapacitor using Ni foam@MCS@NCS as positive electrode and Ni foam@AC as negative electrode was fabricated. The asymmetric supercapacitor exhibited large operating window, excellent energy density and good cycling stability.

In order to increase the flexibility of a supercapacitor, flexible paper-based supercapacitor electrodes were investigated. A simple and low-cost soaking and electrodeposition method was introduced to coat carbon nanotubes (CNTs) and Ni-Co-S on a filter paper to form flexible paper-based electrodes. The as-prepared NiCoS-CNTs paper-based electrode exhibited excellent areal capacitance due to the synergistic effect from the double layer capacitance of CNTs and the pseudocapacitance of Ni-Co-S. The flexibility of the NiCoS-CNTs paper electrode was also studied. It was found that the cyclic voltammetry curves of the electrode were almost unchanged after various bending cycles. This revealed that the proposed NiCoS-CNTs paper electrode had excellent flexibility and mechanical stability. The

symmetric supercapacitor made by flexible NiCoS-CNTs paper electrodes demonstrated great promise for flexible energy storage applications.

Lastly, solid-state flexible supercapacitor based on inkjet-printed interdigital electrodes was studied. Inkjet printing technology is essential for the realization of scalable energy storage. A printable pseudocapacitive ink consisted of Mn^{2+} and Co^{2+} was prepared and deposited on a thin Al foil by inkjet printing to form interdigitated electrodes. Symmetric supercapacitors with different dimensions of interdigitated electrodes were fabricated and characterized. The space-length-width of the electrode fingers could significantly influence the total surface area of the electrodes, thus the electrochemical characteristics.